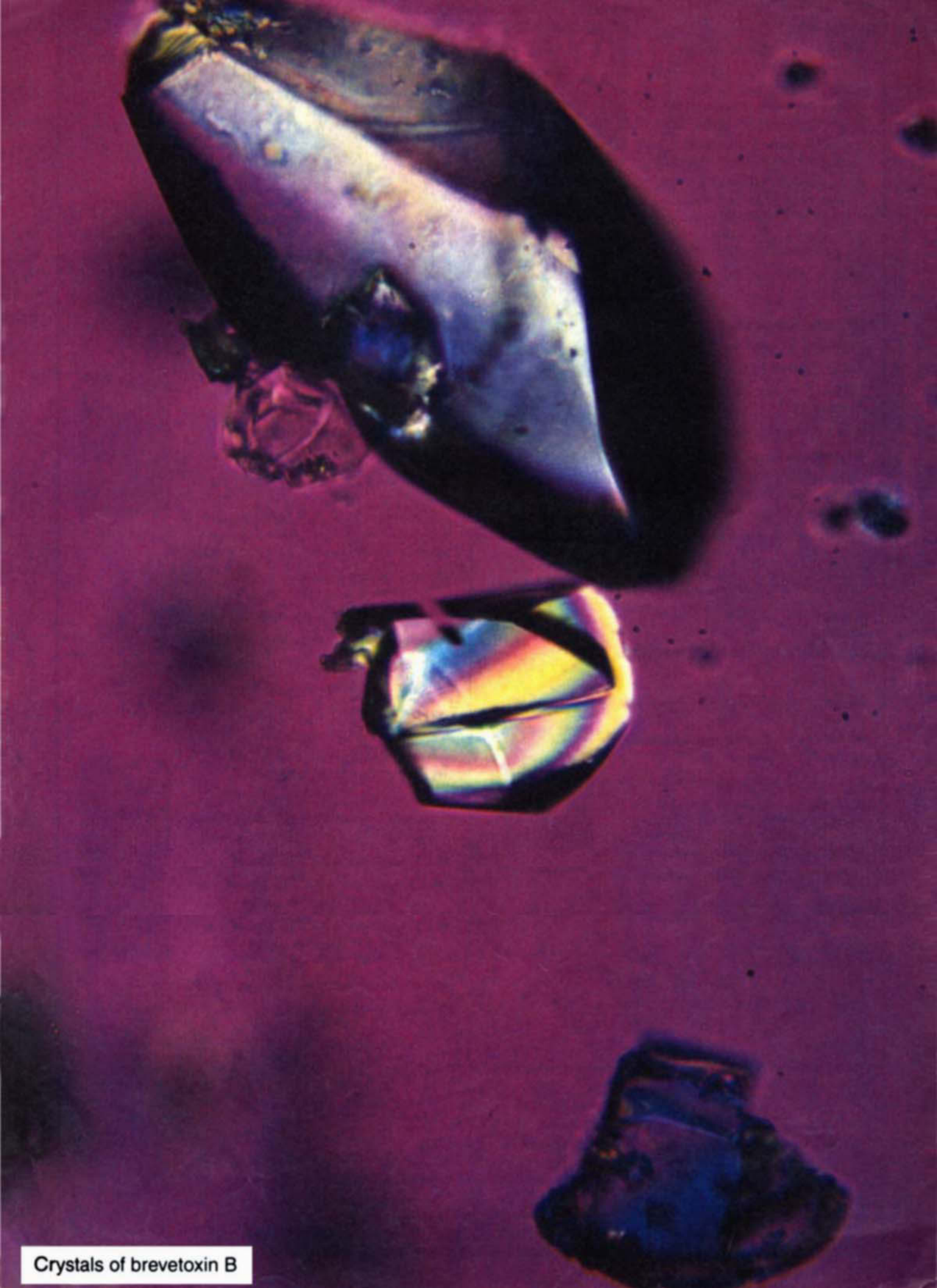

Crystals of brevetoxin B

Understanding and Manipulating Inorganic Materials with Scanning Probe Microscopes

Charles M. Lieber,* Jie Liu, and Paul E. Sheehan

Scanning probe microscopies, such as scanning tunneling microscopy and atomic force microscopy, are uniquely powerful tools for probing the microscopic properties of surfaces. If these microscopies are used to study low-dimensional materials, from two-dimensional solids such as graphite to zero-dimensional nanostructures, it is possible to elucidate atomic-scale structural and electronic properties characteristic of the bulk of a material and not simply the surface. By combining such measurements with chemical synthesis or direct manipulation it is further possible to elucidate relationships between composition, structure, and physical properties, thus promoting an understanding of the chemical basis of material properties. This article illustrates that the combination of scanning probe microscopies and chemical synthesis has advanced our understanding of charge density waves, high-temperature superconductivity, and nanofabrication in low-dimensional materials. This new approach to studying materials has directly contributed to our knowledge of how metal dopants interact with charge density waves and elucidated the local crystal chemistry of complex copper oxides, microscopic details of the superconducting states in materials with a high superconducting transition T_c, and new approaches to the fabrication of multicomponent nanostructures. Coupling scanning probe microscopy measurement and manipulation with chemical synthesis should provide an approach to understanding material properties and creating complex nanostructures in general.

Keywords: atomic force microscopy · low-dimensional materials · nanosyntheses · scanning tunneling microscopy · superconductivity

1. Introduction

An important goal of condensed matter research is to understand how microscopic or atomic level structural and electronic characteristics of a solid determine observable properties like superconductivity and magnetism. This goal is motivated by the recognition that such an understanding will enable scientists to design bulk solids and nanostructures having predictable properties rationally. For chemists, instrumental methodologies that provide a real-space picture of the connectivity of atoms in a solid or of the local electronic structure are perhaps most appealing, since our training in chemistry typically focuses on the direct analysis of the properties of isolated molecules and macromolecules and not the inverse (that is, reciprocal space) analysis of periodic ensembles of atoms and molecules. Furthermore, real-space probes are required to assess the intrinsic structural and electronic properties of very small material structures that are a focus of the burgeoning area of nanotechnology.

Scanning tunneling microscopy (STM), atomic force microscopy (AFM), and other scanning probe microscopies (SPMs) are uniquely powerful tools for probing the microscopic properties of materials.[1-12] STM can be used to probe the surface structure and electronic states of conducting and semiconducting materials directly on the atomic scale,[1-3,9] while AFM can be used to assess the structure and elastic properties of insulators, semiconductors, and conductors at the nanometer scale.[2,4-6,10-12] SPMs are also effective tools for manipulating matter on the atomic to nanometer scales and for constructing individual nanostructures.[9-11,13,14] Additionally, these techniques represent one of the best approaches for relating nanoscale structures to the world we can visualize.

SPMs are, by their very nature, highly surface-sensitive techniques. The ability to probe the uppermost layers of a material is an important advantage in studies of very small supported structures, such as nanocrystals on surfaces, and in fundamental investigations of growth and catalysis on metal and semiconductor surfaces.[15-17] Surface sensitivity can, however, be a severe limitation in studies designed to probe the bulk properties of a material. For example, the coordinatively unsaturated surface atoms of three-dimensional (3D) solids typically adopt a different geometrical arrangement from those in the bulk (that is, they reconstruct). However, highly anisotropic materials—for example, layered solids possessing strong covalent bonding

[*] Prof. C. M. Lieber, J. Liu, P. E. Sheehan
Department of Chemistry and Division of Applied Sciences
Harvard University, Cambridge, MA 02138 (USA)
Fax: Int. code +(617) 496-5442

  0570-0833/96/3507-0687 $ 15.00+.25/0

in two-dimensional (2D) sheets with weak noncovalent bonds holding these layers together—cleave preferentially along planes defined by the weak noncovalent bonds. The coordination of atoms at the surface cleavage plane in such low-dimensional solids is similar to that in the bulk, since the covalent bonding is unchanged, and thus these surfaces do not reconstruct. SPM studies of such low-dimensional materials offer the opportunity of probing atomic level structural and electronic properties that are representative of the bulk of a material.

Low-dimensional solids offer a great richness and complexity of physical phenomena that make them generally an important focal point of condensed matter research. For example, many two-dimensional and one-dimensional metal chalcogenide materials exhibit complex charge density wave and spin density wave phases, and furthermore, the layered structure of the copper oxide superconductors is central to the high-temperature superconductivity that these materials exhibit. This review highlights first the application of SPM techniques to understanding fundamental properties of low-dimensional inorganic materials that exhibit charge density wave and superconducting states. By utilizing these microscopies often combined with systematic chemical modifications, new and unique insight into the properties of these materials has been gained that goes far beyond that obtained with more conventional approaches. Secondly, this review will also focus on the use of SPMs to manipulate inorganic systems. Direct manipulation of atoms and clusters enables the construction of new low-dimensional materials—nanostructures—that can then be investigated by SPM techniques in a nonperturbative mode.

2. Background: Scanning Probe Microscopies

2.1. Scanning Tunneling Microscopy

The scanning tunneling microscope was invented by Binnig and Rohrer in the early 1980s[1] and is now a widely used tool in many fields of research.[1-16] Here we briefly review key features of STM and the theoretical underpinning necessary to understand the investigations discussed below. The basic design of a scanning tunneling microscope is illustrated in Figure 1.

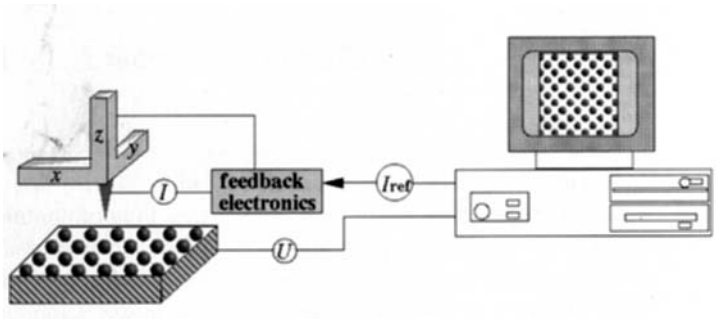

Fig. 1. Schematic diagram of a scanning tunneling microscope.

The essential components include a sharp metal tip, which acts as the local probe, a sample with a conducting surface, a system for positioning the probe in the x, y, and z directions that uses piezoceramic drivers, a feedback loop for controlling the separation between tip and sample with subangstrom precision, and an overall controller that drives the scanner while recording the surface image.

C. M. Lieber

J. Liu

P. E. Sheehan

Charles M. Lieber obtained his early education in New Jersey. He completed a B. A. with honors in chemistry in 1981 at Franklin and Marshall College, earned his Ph.D. at Stanford University under the direction of N. S. Lewis, and carried out postdoctoral research at the California Institute of Technology under H. B. Gray. He is currently a Professor at Harvard University, where he is a member of the Chemistry Department and Division of Applied Sciences. His research integrates several disciplines, including inorganic, physical and materials chemistry, condensed matter physics, and materials science. His research group has been using scanning probe microscopies and other new techniques combined with materials synthesis to understand and control the fundamental properties of materials.

Jie Liu was born in Shandong, China, in 1968. He received his B. Sc. and M. S. degrees from Shandong University in 1987 and 1990. He is currently a graduate student in Professor Lieber's research group at Harvard, investigating the structural and electronic properties of low-dimensional materials, including high-T_c superconductors and transition metal dichalcogenides.

Paul E. Sheehan was raised and educated in North Carolina. He received his B. S. in Materials Science in 1993 from the University of North Carolina-Chapel Hill. He is currently a graduate student in Professor Lieber's research group at Harvard, pursuing the mechanics and tribology of nanoscale structures.

The underlying basis for the operation of the microscope is electron tunneling between a sharp metal tip and a conducting sample.[1-3] When the tip and sample are brought sufficiently close (5–10 Å), their wave functions can overlap. If a bias voltage U is then applied to the sample, a tunneling current I will flow between the sample and tip. Electrons will tunnel from filled electronic states in the tip to empty states in the sample when U is positive, and from filled sample states to empty tip states when U is negative. The tunneling current that flows when U is applied varies exponentially with the tip–sample separation, and for typical work functions decreases tenfold for an increase of one angstrom in separation. The strong exponential dependence of the tunneling current on distance enables STM to achieve high vertical resolution. An atomic resolution map of the surface can then be generated by rastering the tip over the sample with control in the angstrom range provided by the piezoceramic positioners. Under favorable conditions, a vertical resolution of hundredths of an angstrom and a lateral resolution of about one angstrom can be achieved.

There are two principal modes of surface imaging with the STM: constant current and constant height. In the constant current mode, the feedback loop controls the vertical position of the tip above the sample so that I is equal to a reference current at all coordinates on the surface. Features in constant current mode images thus correspond to vertical displacements of the positioner needed to maintain a constant tunneling current. In constant height mode imaging the tip height above the surface is constant, and images correspond to the variation of I with position. Since the feedback loop does not respond to rapid height variations in this mode, it is possible to scan at a higher rate than in the constant current mode. The constant height mode is, however, limited to flat samples.

To interpret STM data requires an understanding of the response of the tunneling current to a number of factors, including applied voltage, tunneling barrier height, and the sample's electronic structure.[2e, 3] As first discussed by Tersoff and Hamann, an expression for I can be readily derived by using perturbation theory to treat the interaction between sample and tip wave functions.[18] In the limit of small bias voltage and low temperature this treatment yields Equation (a), where M_{st} is the tunneling matrix element between wave functions on the tip (Ψ_t) and sample (Ψ_s). As shown by Bardeen,[19] the tunneling matrix element can be written as Equation (b), where the integral corresponds to a surface within the barrier region between the sample and tip. To evaluate M_{st} in a way that the resulting expression for I can be compared quantitatively to STM images in general (that is, not for one specific choice of sample and tip) requires several approximations. Tersoff and Hamann showed that by assuming that the tip forms a locally spherical potential well with only s-wavefunctions, I could be expressed as (c).

$$I = (2\pi/\hbar)e^2 U \sum |M_{st}|^2 \delta(E_s - E_f)\delta(E_t - E_f) \quad (a)$$

$$M_{st} = (\hbar^2/2m) \int (\Psi_t^* \nabla \Psi_s - \Psi_s \nabla \Psi_t^*) dS \quad (b)$$

$$I \sim \sum_s |\Psi_s(r_0)|^2 \delta(E_s - E_f) \quad (c)$$

By definition the summation is the local density of sample electronic states, $\rho(r_0,E)$, at the center of curvature of the tip (d).

Thus, constant current images correspond simply to contours of constant density of sample electronic states.

$$\rho(r_0,E) \equiv \sum_s |\Psi_s(r_0)|^2 \delta(E_s - E_f) \quad (d)$$

It is useful to consider the effect of the approximations made in deriving (d). Treatment of the tip's potential as spherical is reasonable, because although the experimental tip shape is generally unknown, it probably terminates in a cluster of atoms; that is, the tip is approximately spherical. The s-wavefunction approximation for the tip is even more significant, because it leads to a cancellation in Equation (b) which makes I dependent only on the square of the sample wavefunction with no contribution from the tip. Tersoff has examined more general descriptions of the tip and found that constant current images still correspond to contours of constant density of sample electronic states for metals.[20, 21] STM images of semiconductor surfaces at low U could, however, deviate significantly from this simple picture, since only a small pocket of the surface Brillouin zone contributes to the tunneling. This deviation is limited, however, to the lowest Fourier component of the image, and thus the model of the tip approximated by an s-wavefunction may still be used in many cases to interpret images at higher bias voltages. While these results indicate that the assumptions used to derive (d) are reasonable, it is important to develop further theoretical models so that data can be quantitatively interpreted.[6, 22]

The dependence of the tunneling current on applied bias voltage, which corresponds to tunneling spectroscopy, can probe the local density of electronic states versus energy, since I is proportional to the local density of states. For finite voltages (c) can be rewritten as (e), where $T(E,eU)$ is the transmission probability that takes into account the energy-dependent wavefunction decay. This expression incorporates the assumption that the density of tip states does not vary significantly with energy. In the limit of small bias, dI/dU is proportional to the density of states; however, for finite bias the exponential dependence of $T(E,eU)$ on U becomes important. This exponential dependence can be effectively removed by normalizing dI/dU by U/I[23] [expression (f)].

$$I \sim \int \rho(r,E) T(E,eU) dE \quad (e)$$

$$(U/I) dI/dU \sim \text{LDOS} \quad (f)$$

Comparisons of the local density of states data obtained by STS with photoemission and inverse photoemission results show that the approximations made in arriving at (f) are reasonable.

2.2. Atomic Force Microscopy

The atomic force microscope, which was invented several years after STM,[10] is now perhaps the most widely used probe microscopy technique.[4-6, 11, 12, 24] The underlying basis for

force microscopy is similar to a simple profilometer;[25] that is, the forces on a probe tip attached to a cantilever are detected and plotted as a sample is scanned beneath the tip. The magnitude of the load in force microscopy is, however, many orders of magnitude smaller than those applied with a conventional profilometer: 10^{-13} to 10^{-6} versus 10^{-4} N. The combination of small loads with sharp tips enables AFM to image at close to atomic resolution. Importantly, force microscopy can, in principle, be used to probe the structure of any solid material, be it a conductor, an insulator, or a living cell, since this technique relies solely on the mechanical interaction between the tip and sample.

The basic design of a modern force microscope is illustrated schematically in Figure 2. The essential components that differ

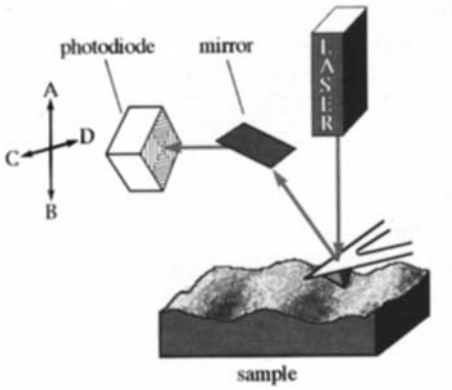

Fig. 2. Illustration of a force microscope that utillizes optical detection.

from those shown for the tunneling microscope (Fig. 1) include an integral tip-cantilever assembly and optical detection system that measures the cantilever deflection. Since the cantilever (spring) deflection is linearly related to the force, the experimental signal is a measure of the force. In operation, variations in the cantilever position, which result from sample topography and/or differing sample–tip interaction, lead to a deflection of the laser beam on a quadrant photodiode detector. By measuring the vertical (A–B) and horizontal (C–D) displacements on the photodiode it is possible to extract both normal and lateral forces. Furthermore, if the normal and lateral spring constants of the cantilever are known, it is possible to quantify these forces from the measured cantilever displacements.[24]

There are several common modes of imaging in contact-mode force microscopy, including constant normal force and lateral force. In the constant-force mode, which is analogous to constant-current mode of STM, the feedback loop controls the vertical position of the sample so that the cantilever displacement and hence normal force is constant at all points on the surface. Features in images recorded in constant-force mode thus correspond to vertical displacements of the positioner needed to maintain a set force between the cantilever–tip assembly and sample surface. In the lateral-force mode, the frictional or lateral force between the tip and sample is mapped as a function of x, y coordinates for a constant applied load. Thus, the constant-force mode of imaging provides a good measure of surface structure, while the lateral-force mode provides indirect information about variations in surface composition (reflected by variations in friction).

3. Quasi-Two-Dimensional Transition Metal Dichalcogenides

3.1. Basic Structure

The dichalcogenides of transition metals of Groups IV, V, and VI have layered structures in which the transition metal (M) occupies either octahedral or trigonal prismatic sites between two layers of hexagonal close packed chalcogenide atoms (X). The X-M-X sandwiches are then stacked in a direction perpendicular to the chalcogenide layer to complete the structure.[26] The octahedral coordination of Ta atoms in 1T-TaS_2[*] is schematically shown in Figure 3. In general, the X-M-X layers are held together by strong covalent or ionic bonding, whereas the interactions holding the layers together are much weaker dispersion forces. These materials cleave readily between the weakly bonded layers to yield free surfaces that are structurally and electronically similar to the bulk material.[7, 8, 26–29]

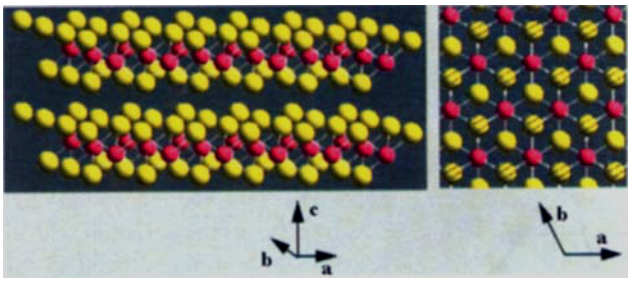

Fig. 3. Schematic side view (left) and top view (right) of 1T-TaS_2. White bonds between yellow sulfur and magenta tantalum atoms highlight the octahedral coordination of tantalum. In the top view, the upper sulfur layer (solid yellow), tantalum, and lower sulfur layer (yellow with black lines) are superimposed.

3.2. Charge Density Waves

The d^1 transition metal dichalcogenide materials exhibit rich temperature-dependent structural and electronic properties. Electronically, the partially filled t_{2g} conduction band in a d^1 system should give rise to metallic conductivity. Indeed, at high temperatures the compound 1T-TaS_2 is metallic; however, on cooling below 543 K 1T-TaS_2 exhibits four distinct temperature-dependent charge density wave (CDW) states.[8, 27, 28] A schematic diagram of the CDW and atomic lattice in 1T-TaS_2 is shown in Figure 4. In general, CDWs are found in low-dimensional systems that exhibit significant Fermi surface nesting (nesting refers to the condition that a piece of the solid's Fermi surface may be translated and superimposed on another piece by a wave vector $\boldsymbol{q}$). Fermi surface nesting leads to a divergence

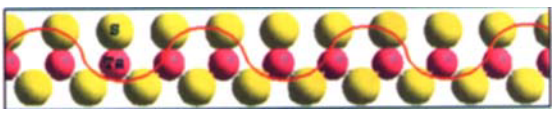

Fig. 4. Cross sectional view of a CDW (sinusoidal red line) in a single layer of TaS_2.

[*] The notation 1T indicates the polytype in which all tantalum atoms are octahedrally coordinated.

in the electronic susceptibility at the q, and through electron–phonon coupling can yield a stable periodic modulation of the atomic lattice and of the electron density in the conduction bond; that is, a CDW. The wavelength (λ) of the CDW is governed by q. Since λ is determined by the Fermi surface size through q, it might not correspond to an integral number of lattice constants (na). In the case where $\lambda \neq na$ the CDW is called incommensurate; however, when $\lambda = na$ it is commensurate.

Prior to the advent of STM the structure of the CDW phases in TaS_2 and other materials had been investigated by X-ray and electron diffraction methods. These techniques showed in 1T-TaS_2 that the high temperature CDW was incommensurate, and that for $T < 183$ K the CDW rotated 13.9° relative to the atomic lattice to become commensurate.[27–29] The real-space structures of these phases are illustrated schematically in Figure 5.

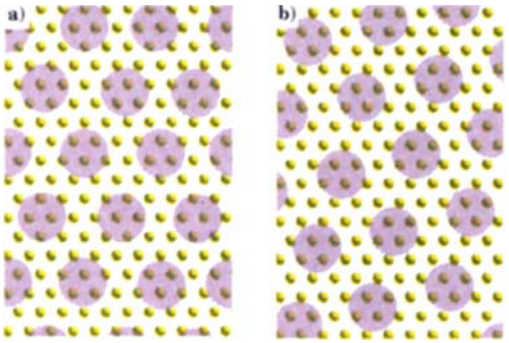

Fig. 5. Schematic top views of the incommensurate (a) and commensurate (b) CDW phases in 1T-TaS_2. The CDW maxima are indicated by pink-shaded circles and the atomic lattice by yellow spheres.

The CDW superlattice of both phases has a regular hexagonal symmetry. In the incommensurate phase the peaks of CDW are located randomly relative to the atomic lattice. In the commensurate phase, the CDW superlattice rotates 13.9° relative to the atomic lattice and expand by 2% with the result that each CDW maximum is oriented over a similar atomic lattice site. Unfortunately it was not possible to resolve the structures of the intermediate-temperature nearly-commensurate and triclinic nearly-commensurate CDW phases by means of diffraction techniques. These two phases had been suggested to exhibit either uniformly incommensurate structures or domainlike structures.[30, 31]

The first application of STM to CDWs was carried out by Coleman and co-workers in 1985.[32] Significantly, this work showed that the charge modulation of a CDW and atomic lattice could be viewed simultaneously in real space. In addition, comparison of early STM data with previous diffraction results demonstrated that the surface-sensitive STM experiment truly reflected the bulk properties of 1T-TaS_2.[32, 33] The ability of STM to determine simultaneously both CDW and atomic lattice positions has subsequently been exploited to resolve the complicated structural details of the intermediate-temperature CDW phases in TaS_2 that previously could not be determined by diffraction techniques.[6, 7, 34–38]

STM studies of the real-space structure of TaS_2 at room temperature showed that the nearly-commensurate CDW phase adopts a novel, hexagonal, domainlike structure, in which there is a periodic variation in the CDW amplitude that occurs on a wavelength much larger than the CDW wavelength λ (Fig. 6).[34] In images of large areas the CDW maxima (Fig. 6a, filled white circles) define a regular hexagonal superlattice with an average wavelength that is consistent in diffraction and STM measurements. The amplitude of the CDW maxima further exhibits a larger periodic modulation that defines domains consisting of relatively high-amplitude CDW maxima separated by lower amplitude domain boundaries. The roughly circular, high-amplitude domains are arranged in a hexagonal superstructure with a period of approximately 70 Å at room temperature. Hence, the nearly-commensurate CDW exhibits a fascinating hierarchy of structures: the hexagonal atomic lattice with period 3.35 Å, the fundamental hexagonal CDW lattice with period of about 12 Å, and the hexagonal domain superlattice with period 70 Å.

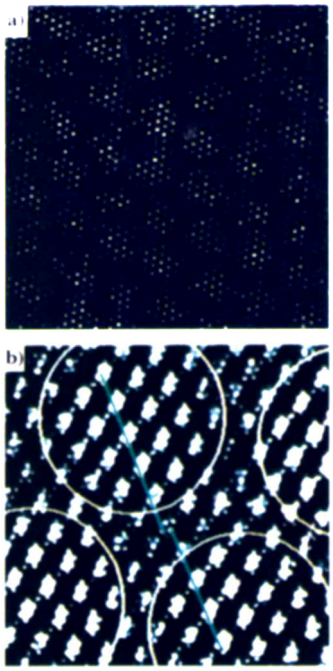

Fig. 6. STM images of 1T-TaS_2 at room temperature: a) 50×50 nm^2 surface showing CDW maxima and domains; b) atomic-resolution imge of four domains.

Images with atomic resolution of the nearly-commensurate phase have provided further insight into the complex structure of the domain phase; four domains are highlighted by white circular lines in Figure 6b. This image shows well-defined phase shifts of one atomic lattice period between the CDWs in adjacent domains:[34, 35, 38] the green lines indicating the CDW directions in adjacent domains have a one-atom mismatch. The abrupt changes in CDW phase are clear in real-space images, but are quite difficult to detect in diffraction measurements. Furthermore, the high-resolution images show a similar arrangement of atoms at each CDW maximum within a domain, thus indicating that the CDW is approximately commensurate (see for example, schematic representation in Fig. 5) in the domains. Because the actual angle between the atomic lattice and CDW superlattice can be measured, such images also enable the issue of commensurability to be addressed quantitatively. Significantly, these measurements showed the angle within single domains was that expected for a commensurate CDW (approximately 13.9°). Taken together, these STM studies unambiguously resolved the long standing controversy about the structure of the nearly-commensurate CDW phase in 1T-TaS_2.

Temperature-dependent SPM measurements are also important for probing CDW phases in the transition metal dichalcogenides further, since temperature variations can be used to assess melting and other phase transitions.[33, 35, 36] STM studies of the nearly-commensurate phase in 1T-TaS_2 first demonstrated the power of such measurements.[35] Images recorded

between 200 and 350 K exhibit the hexagonal CDW domain structure described above. The period of the domain structure was found to undergo a remarkable and unexpected change with temperature decreasing from 100 Å at 200 K to approximately 60 Å at 350 K (Figs. 7a–c). At still higher temperatures, there is an abrupt loss of the domain structure as the true incommensurate phase is formed (Fig. 7d). Significantly, the decrease in domain size appears similar to a second-order melting transition as the sample temperature is raised; however, it is important to point out that this corresponds to melting of an electronic (CDW) lattice and not the atomic lattice.

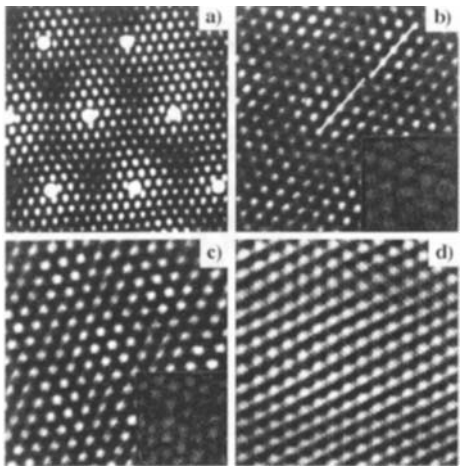

Fig. 7. STM images of 1T-TaS_2 recorded at sample temperatures of 242 (a), 298 (b), 349 (c), and 357 K (d). The imaged surfaces are 30×30 (a), 17.5×17.5 (b), and 15.5×15.5 nm^2 (c and d). The insets in b) and c) are 30×30 nm^2. The domain center positions for an ideal hexagonal structure are marked with white dots in a).

3.3. Role of Metal Substitution

From a chemist's perspective one of the most exciting areas of SPM-related materials research is that focusing on understanding how chemical substitutions or doping affect the structural and electronic properties of a solid at the atomic level. In the specific case of materials with CDWs, the crucial issue is to understand how a CDW interacts with the metal impurities doped into the atomic lattice, since the nature of the interaction between impurities and a CDW controls both the static and dynamic properties of the CDW state.[39–45] CDW pinning can, in general, be classified as either strong or weak depending on the competing energetics of the CDW–impurity interaction and the CDW deformation energy (Fig. 8).[39, 41, 42] In strong pinning, the impurity's potential dominates the CDW elastic energy and pins the phase of the CDW at each impurity site. In weak pinning, the CDW breaks up into constant phase regions that are pinned collectively by impurities. Despite the fundamentally different structural manifestations of strong and weak pinning, there has been considerable controversy concerning the nature of pinning in CDW systems.[39–49] This controversy has been due in large part to the lack of data characterizing the evolution of CDW structure with impurity doping. Real-space imaging of the CDW structure in doped materials by STM has, however, addressed and resolved directly the important issue of strong versus weak pinning.[8, 50–57]

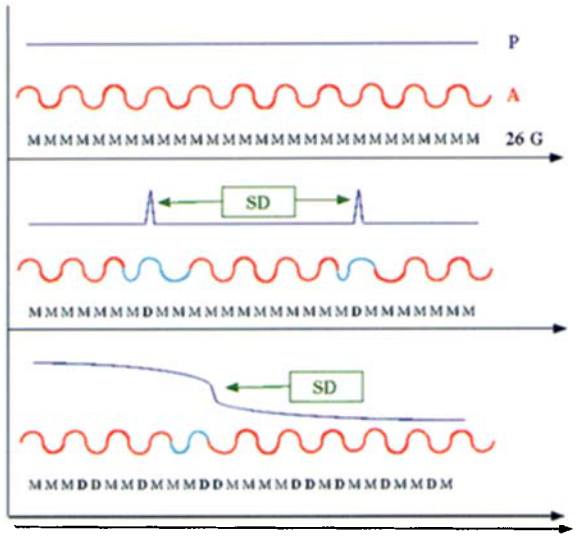

Fig. 8. Plots of the CDW phase and amplitude as a function of lattice position for a perfect one-dimensional lattice (top), a lattice containing strong pinning impurities (middle), and a lattice containing weak pinning impurities (bottom). A = CDW amplitude, L = lattice, P = CDW phase, SD = structural defect. D in the lattice represents dopant molecules.

We have investigated the effect of impurities through systematic studies of metal-substituted tantalum disulfide, $M_xTa_{1-x}S_2$, where M atoms randomly replace Ta sites in the lattice.[50–57] In principle, substitution of isoelectronic Nb^{IV} for Ta^{IV} centers represents the weakest perturbation on the potential that is possible with metal substitution, and thus serves as the best test of the weak pinning regime. The effect of Nb-substitution on the macroscopic transport properties of these $Nb_xTa_{1-x}S_2$ materials has been assessed by variable-temperature resistivity measurements.[27, 28] Nb-substitution (and other metal substitutions) decreases the transition temperature from the high-temperature incommensurate CDW state to the lower temperature nearly-commensurate state. Qualitatively, the suppression in the transition temperature can be rationalized by assuming that the incommensurate state is stabilized by impurity pinning. Structural studies of these same materials with electron diffraction confirmed that the Nb-impurities pin the incommensurate CDW, but could not provide information about the nature of pinning.[27] STM images do, however, provide direct insight into the structural effects and mechanism of pinning.

STM images of $Nb_xTa_{1-x}S_2$ single crystals with values of x ranging from 0 to 0.07 are shown in Figure 9. The images were recorded at the elevated temperatures of 380 K ($x = 0$), 340 K ($x = 0.04$), and 315 K ($x = 0.07$) to ensure that the samples were in the incommensurate state, where the CDW interacts only weakly with the underlying lattice.[53, 57] Pure TaS_2 exhibits a nearly perfect hexagonal CDW lattice that is characteristic of the known incommensurate state in this material. In contrast, substitution with niobium causes disorder in the CDW lattice. The images of the Nb-doped materials exhibit areas in which the CDW lattice has hexagonal order and regions containing defects. These defects introduce disorder into the CDW lattice. The predominant defects observed in the samples in which $x(Nb) < 0.07$ are dislocations. Dislocations are formed by the insertion of extra half rows of CDW sites in the lattice. Importantly, there is a significant strain field associated with the dislo-

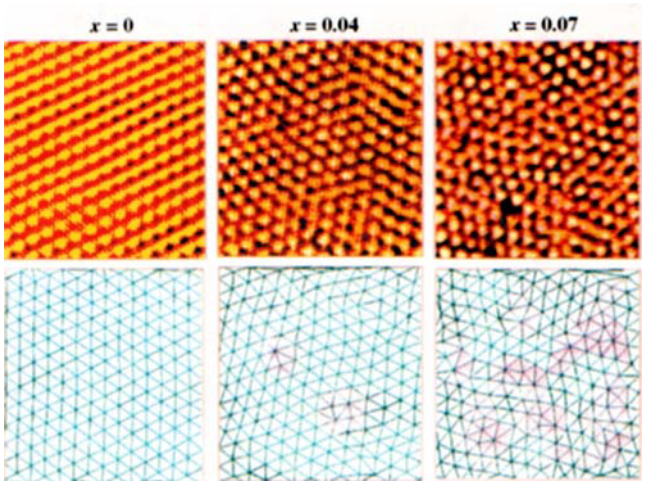

Fig. 9. STM images of the $Nb_xTa_{1-x}S_2$ crystals recorded at 380 ($x = 0$, 340 ($x = 0.04$) and 315 K ($x = 0.07$). Delaunay triangulations are shown below the corresponding STM images.

cations.[58] The CDW can relax the strain field by locally deforming through positional shifts and rotations, although these deformations introduce disorder into the lattice. In the samples containing higher impurity concentrations (x(Nb) ≥ 0.07) STM images exhibit extended defects. The CDW lattice in these latter samples exhibits significant disorder, and regions of hexagonal order and positional order extend only several lattice constants. Nevertheless, it is important to note that the disorder does not appear to destroy the orientational order of the CDW lattice. The presence of relatively long-range orientational order can be seen qualitatively by sighting down the rows of the CDW lattice: this shows that the average direction is defined regardless of the Nb impurity concentration.

To examine in more detail the order of a lattice it has been instructive to analyze the images quantitatively. The quantitative analysis involves defining the location (x, y coordinates) of each CDW maxima and the nearest neighbors in the lattice. Once the lattice points are determined, the Voronoi diagram, which uniquely defines the nearest neighbors of all lattice points, is computed for the lattice.[59] To highlight defects in the lattice we triangulate the Voronoi diagram by drawing "bonds" from all CDW lattice points to their nearest neighbors.[55, 57, 59] This resulting plot is termed the Delaunay triangulation. For the CDW lattice, fully coordinated sites are indicated by six bonds, while topological defects containing a smaller or greater number of bonds are highlighted by shading. The triangulated images are shown below their corresponding STM images in Figure 9; the topological defects are shaded pink. These data demonstrate clearly that the pure 1T-TaS_2 CDW lattice is defect free and that the number of topological defects increases with increasing Nb impurity concentration. Significantly, analysis of the average spacing between topological defects shows that it is much greater than the average spacing between Nb impurities, and thus this analysis unambiguously shows that the pinning by Nb atoms is a weak or collective effect.[8]

It is also possible to obtain further insight into the changing order in this system by calculating the translational [$G_T(r)$] and orientational [$G_6(r)$] correlation functions for a two-dimensional lattice.[8, 55, 59, 60] Significantly, analyses of $G_T(r)$ and $G_6(r)$ as a function of the Nb impurity concentration show that 1) for $x = 0$, both $G_T(r)$ and $G_6(r)$ exhibit long-range order; 2) for $0 < x \leq 0.04$, $G_T(r)$ decays exponentially (which indicates short-range order), and $G_6(r)$ exhibits long-range order; and 3) for $x \geq 0.07$, $G_T(r)$ and $G_6(r)$ decay exponentially. The existence of long-range orientational order but short-range translational order was an important observation, because it showed the existence of a hexatic glass state in these doped materials.[55, 59, 60] Hence, these microscopic STM studies led to the unexpected discovery that the CDW lattice evolves from a crystalline state in the pure solid through a hexatic glass state to a liquid-like amorphous state as the impurity concentration increases.

A very different impurity pinning effect has been observed in our STM studies of titanium-doped $TaSe_2$.[54] The CDW state in 1T-$TaSe_2$ is commensurate at all experimentally accessible temperatures, and each CDW maximum is located on a similar symmetric Ta atom site (Fig. 5b) effectively pinning the CDW to the underlying atomic lattice. The driving force for the commensurate state is an electrostatic interaction between the Ta ions and the CDW. In the incommensurate state, this electrostatic pinning term would be zero. The strong interaction between the CDW and atomic lattice that exists in the commensurate state suggests that the added pinning effect of metal impurities should be quite different than observed in the above studies of $Nb_xTa_{1-x}S_2$. STM images recorded on a series of $Ti_xTa_{1-x}Se_2$ single crystals with $x = 0$, 0.02, and 0.04 support this idea (Fig. 10). The CDW lattices observed in samples containing

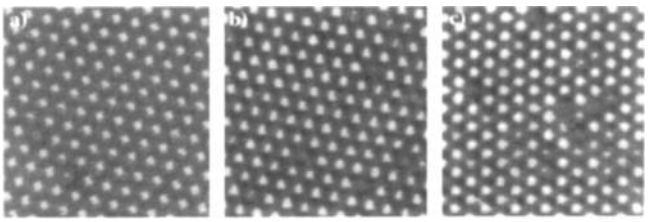

Fig. 10. STM images ($13.5 \times 13.5\ nm^2$) of $TaSe_2$ (a), $Ti_{0.02}Ta_{0.98}Se_2$ (b), and $Ti_{0.04}Ta_{0.96}Se_2$ samples (c) recorded at room temperature.

titanium impurities exhibit a regular hexagonal structure that is similar to the pure sample. The overall order in the CDW lattice of the Ti-doped materials thus differs significantly from that observed in the $Nb_xTa_{1-x}S_2$ materials where the niobium impurities create substantial disorder in the CDW superlattice. The images of the Ti-doped materials do, however, exhibit localized regions where the CDW amplitude is suppressed relative to the surrounding CDW maxima. In addition, we have shown that the density of these localized defects increases linearly with the titanium impurity concentration. These data and the highly localized nature of the CDW defects represent solid evidence for strong pinning.

The studies of $Nb_xTa_{1-x}S_2$ and $Ti_xTa_{1-x}Se_2$ demonstrate the power of STM in elucidating complex structural problems in these CDW materials. It is also possible that detailed spectroscopic studies of single CDW defects at strong pinning sites will provide unique information relating to the microscopic details of CDW formation. In particular, it should be possible to probe the symmetry properties of the CDW gap by probing electron

scattering at CDW defect sites. Careful analysis of the symmetry and decay of the charge density around the defects, which is measured in voltage-dependent STM images, should provide unique information about the Fermi surface topography and scattering in these materials.

4. Copper Oxide Superconductors

4.1. $Bi_2Sr_2Ca_{n-1}Cu_nO_{2n+4}$ Materials: The Incommensurate Superstructure

The copper oxide superconductors are highly anisotropic materials containing two-dimensional copper oxide planes as a key structural element.[61-63] The other components of these materials determine the overall structural anisotropy, chemical complexity, and ultimately the superconducting transition temperatures T_c of these materials. Among the high-temperature superconductors now known, the $Bi_2Sr_2Ca_{n-1}Cu_nO_{2n+4}$ family of materials ($n = 1-3$) are the most anisotropic and probably best suited to surface-sensitive experiments. The $n = 2$ compound, $Bi_2Sr_2CaCu_2O_8$ (BSCCO-2212), is structurally representative of this family and consists of two-dimensional repeat units containing 2-BiO, 2-SrO, Ca, and 2-CuO_2 layers (Fig. 11).[61a, 63, 64]

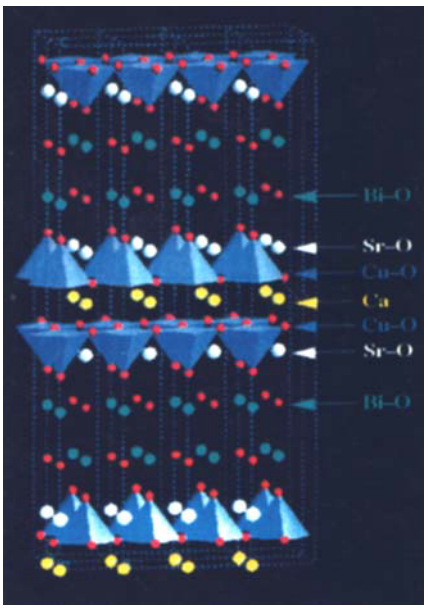

Fig. 11. Structural model of $Bi_2Sr_2CaCu_2O_8$.

The average structure of BSCCO-2212 obtained from diffraction studies is quite straightforward, although in reality these materials exhibit a wide range of structural complexities.[64, 65] For example, BSCCO-2212 shows considerable disorder in the atomic structure of the BiO layer, oxygen nonstoichiometry, and exchange of metals between the idealized layers shown in Figure 11. The detailed nature of such local disorder is intrinsically difficult to address by conventional diffraction techniques, as are the electronic consequences of these structural variations. A complete picture of the microscopic properties of these materials is, however, almost certainly necessary to understand high-temperature superconductivity, since the structural disorder has a dimensionality similar to the coherence length of the superconducting electron pairs. Moreover, the complex high-T_c materials can also serve as models to understand the role of intricate compositional and structural variations that are present in multicomponent materials in general.

The crystallographic separation between adjacent BiO layers in BSCCO is quite large (greater than 3 Å) and as such provides a natural cleavage plane in crystals of these materials.[63, 64] Because covalent bonds are not broken when cleaving crystals between the weakly interacting BiO layers, the BiO surface layer does not reconstruct; hence, STM experiments probe properties similar to that found in the bulk.[66-68] STM images of cleaved BSCCO-2212 crystal surfaces exhibit structure on several length scales (Fig. 12). Of particular interest has been the one-dimen-

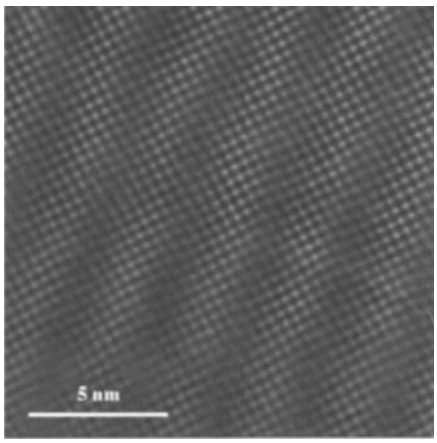

Fig. 12. STM image of $Bi_2Sr_2CaCu_2O_8$ exhibiting the one-dimensional superstructure and BiO layer atomic lattice.

sional superstructure modulation of period 27 Å that occurs along the a axis. A number of models have been proposed to explain the origin of this unique structural modulation in BSCCO, including 1) lattice mismatch between the BiO and CuO layers; 2) extra oxygen atoms substituted into the BiO layer, which causes it to buckle periodically; and 3) periodic Cu or Sr substitution for Bi in the BiO layer.[64, 66, 67, 69, 70] At least three problems intrinsic to these materials have hampered efforts based on diffraction to elucidate the origin of this superstructure. Firstly, the superstructure period is incommensurate with respect to the lattice. Secondly, the BiO layer has considerable disorder, and thirdly, the X-ray and electron scattering cross sections for oxygen are significantly smaller than for Bi.[65, 70]

STM is not limited by these problems and has provided unique insight into the origin and effects of this modulation.[66-68] Real space STM images such as Figure 12 show that the superstructure period is not a sinusoidal modulation; the period varies randomly from 22 to 27 Å.[67] These results demonstrated that the superstructure could not be due simply to BiO/CuO lattice mismatch (which would yield a sinusoidal modulation), but must have a random substitutional component that caused local fluctuations in the superstructure period. Further evidence for the importance of substitution in determin-

ing the properties of the superstructure will be discussed below with relation to metal substitution and oxygen doping.

The atomic structure in images of the BiO layer (for example, Fig. 12) has tetragonal symmetry with a period of 3.8 Å. This distance is consistent with both the average Bi–Bi and O–O distances determined by crystallography; that is, alternate atomic sites, either Bi or O, are imaged by STM. Because only one site is imaged by STM, such data cannot be used to define unambiguously the complete atomic structure associated with the superstructure modulation. The images at atomic resolution do show, however, that there can be significant positional disorder in the BiO layer. We have suggested that this disorder reflects inhomogeneity at the atomic level in the material. Hence, one possible application of STM is the improvement crystal quality achieved by monitoring order in the real-space atomic structure as a function of crystal growth conditions.

4.2. Chemical Inhomogeneity in $Tl_2Ba_2Ca_2Cu_3O_{10}$

The ability of SPM techniques to monitor growth-dependent local atomic order in these complex systems and thereby provide insight into observable properties at a microscopic level is general. Studies of the $Tl_2Ba_2C_{n-1}Cu_nO_{2n+4}$ family of materials ($n = 2, 3$) have clearly illustrated this point.[71, 72] These materials are derived from the Bi family simply by replacing Bi with Tl and Sr with Ba.[61, 63] In general, the average atomic structures of the Tl-based materials are similar to those of the Bi family, although there are several important differences: 1) the Tl materials do not exhibit a regular one-dimensional superstructure and 2) the bonding between adjacent TlO layers is significantly stronger.[61, 63, 73] Despite the stronger bonding between the TlO double layers, crystals of $Tl_2Ba_2CaCu_2O_8$ and $Tl_2Ba_2Ca_2Cu_3O_{10}$ cleave predominantly between the TlO double layers to expose a TlO surface in a manner analogous to that for BSCCO.[71, 72]

The correlation of the microscopic studies by means of STM with macroscopic conductivity measurements have been particularly interesting. Temperature-dependent resistivity measurements made on $Tl_2Ba_2Ca_2Cu_3O_{10}$ crystals grown under various conditions showed strikingly different T_c values (Fig. 13).[72] Crystals grown from a flux containing a Tl:Ba:Ca:Cu ratio of 4:1:3:6 exhibited a broad superconducting transition and a low

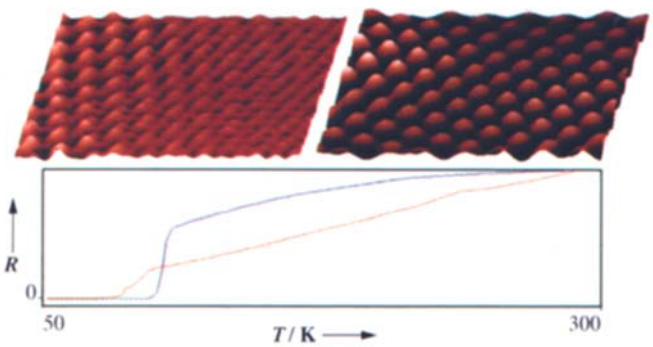

Fig. 13. Top: STM images $Tl_2Ba_2Ca_2Cu_3O_{10}$ crystals grown from 4:3:1:6 (left) and 4:3:1:10 Tl:Ba:Ca:Cu mixtures (right). Bottom: Temperature-dependent resistivity measurements made on $Tl_2Ba_2Ca_2Cu_3O_{10}$ crystals grown under these conditions. R = resistivity.

T_c of 72 K. In contrast, crystals grown from a flux containing a Tl:Ba:Ca:Cu ratio of 4:1:3:10 had a sharp T_c of 110 K. Despite the large differences in T_c, X-ray diffraction and the analysis of the composition showed that these two types of crystals had the same average structure and composition.[61a, 73, 74] The origin of these differences in T_c were, however, readily traced from atomic resolution STM measurements (Fig. 13). The STM images showed clearly that the lower T_c $Tl_2Ba_2Ca_2Cu_3O_{10}$ crystals had pronounced atomic structural disorder, while images of the higher T_c materials exhibited a very regular atomic lattice.[72] These results thus indicate that difference in the macroscopic parameter T_c are due to localized, microscopic variations in the structure of the $Tl_2Ba_2Ca_2Cu_3O_{10}$ samples.

4.3. Metal Substitution: Probing Local Crystal Chemistry

SPM techniques have also been used to probe the effects on the microscopic level of metal substitution in high-T_c copper oxide materials.[7a, 67, 75, 76] In the case of Pb-substituted BSCCO crystals ($Pb_xBi_{2-x}Sr_2CaCu_2O_8$), STM is an especially good probe, since lead primarily replaces bismuth in the BiO layers. The Pb-doped crystals can be cleaved to expose a Bi(Pb)O layer directly at the surface (Fig. 14).[67] STM images

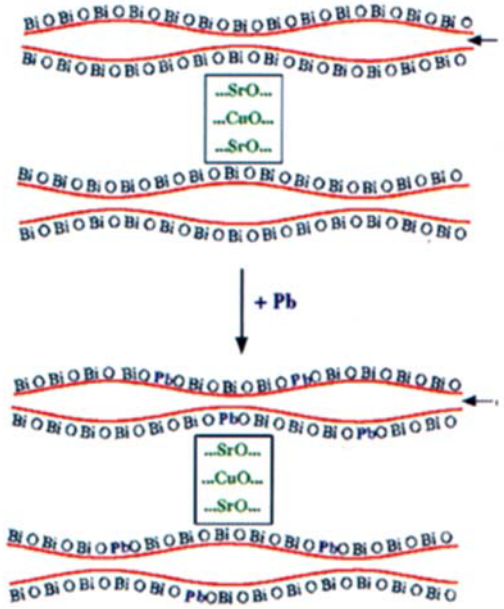

Fig. 14. Schematic illustration of Pb-substitution into the BiO layer of BSCCO-2212. The arrows indicate cleavage planes.

of the Bi(Pb)O layer of Pb-doped BSCCO-2212 single crystals are shown in Figure 15. Images of pure ($x = 0$) BSCCO-2212 crystals exhibit the one-dimensional, incommensurate superstructure that is characteristic of the BSCCO materials.[67, 75] As Pb atoms are substituted for Bi atoms in these crystals, however, the superstructure exhibits increasing disorder. STM images of materials with $x \leq 0.2$ show that the one-dimensional superstructure is less regular than in Pb-doped BSCCO as evidenced by the random displacements along the a axis.[67] The distortions of the superlattice have been attributed to the random substitution of lead for bismuth in the Bi(Pb)O planes and

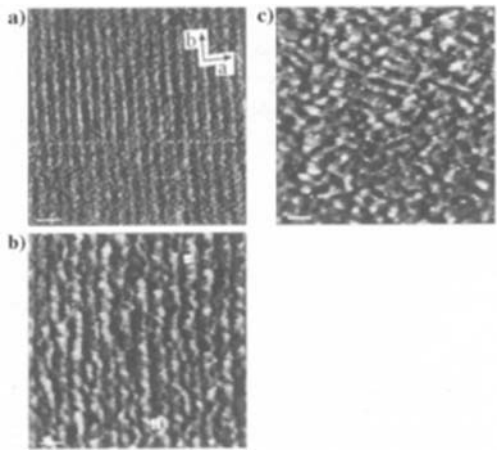

Fig. 15. STM images of $Bi_2Sr_2CaCu_2O_8$ (a), $Pb_{0.3}Bi_{1.7}Sr_2CaCu_2O_8$ (b), and $Pb_{0.5}Bi_{1.5}Sr_2CaCu_2O_8$ (c). The underlying a and b cell axes are indicated in a). The white bar corresponds to 5 nm in these images. The tiny arrows in b) indicate two locations where the superstructure fluctuates significantly from its average position.

the differences between PbO and BiO bonding. Significantly, distortions in the superstructure imaged directly by STM explain the decrease in correlation length reported in diffraction studies of these materials;[77] that is, random fluctuations along the a axis (due to Pb-substitution) reduces the scattering coherence. The suggestion that Pb-substitution distorts the superlattice has been further supported by STM images of samples containing high concentrations of lead (Fig. 15c), since these images exhibit a highly disordered superstructure modulation.

The STM structural data have also provided an understanding of observed variations in the critical current density (J_c) that occur with Pb-substitution. Studies of J_c in Pb-doped BSCCO-2212 have shown that the substitution of lead causes reproducible and significant enhancements in J_c.[78] While it is well known that crystal "defects" can enhance pinning of the fluxlines in superconductors, thereby increasing J_c, the nature of these defects are often not well understood. In the case of Pb-doped BSCCO, the STM images suggest that it is the Pb-induced disorder that enhances flux pinning.

STM studies of crystals of Pb-doped BSCCO-2201, $Pb_xBi_{2-x}Sr_2CuO_6$ single crystals have shown similar results and have been used to develop a new approach for understanding the local disorder probed by SPM measurements.[76] Images of Pb-doped BSCCO-2201 crystals exhibit increasing disorder as the concentration of Pb atoms is increased (Fig. 16). To quantify the order in these crystals and to compare the results to those obtained by electron diffraction we have used the two-dimensional structure factor $S_{2D}(k)$ ($S_{2D}(k) = |\rho(k)|^2$, where $\rho(k)$ is the Fourier transform of the atom density calculated from STM images as function of Pb concentration (Fig. 17). Consideration of this analysis has shown several significant points. Firstly, for samples with intermediate Pb concentrations the comparison of $S_{2D}(k)$ and real-space images with in-plane electron diffraction patterns show that the multiple superlattices inferred from electron diffraction[77] are due to harmonics of the principle superlattice period (Figs. 16b, 17b, e). Secondly, at higher Pb concentrations this same comparison demonstrates that the absence of the one-dimensional superstructure inferred from electron diffraction[79] is due to extreme disorder in this

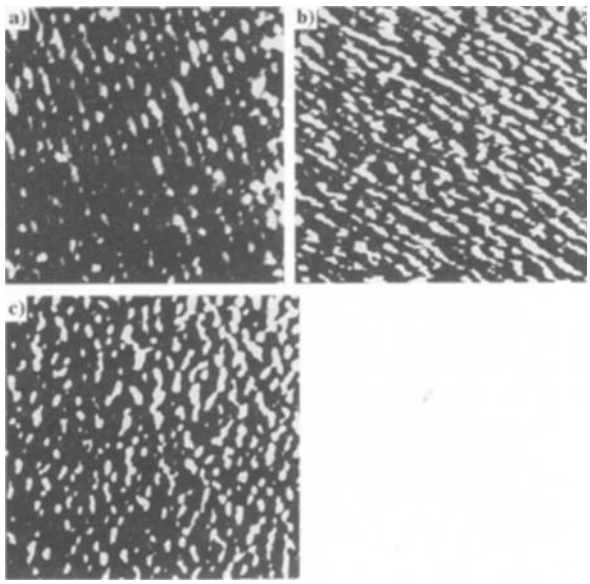

Fig. 16. Images (60×60 nm^2) of $Bi_2Sr_2CuO_6$ (a), $Pb_{0.15}Bi_{1.85}Sr_2CuO_6$ (b), and $Pb_{0.3}Bi_{1.7}Sr_2CuO_6$ (c).

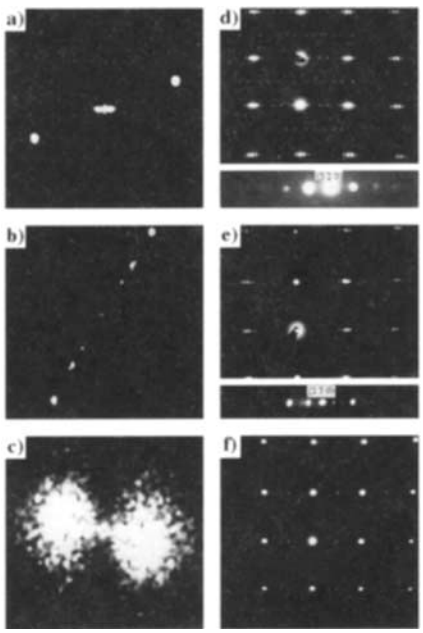

Fig. 17. a)–c): Two-dimensional Fourier transform power spectra of the STM images in Figure 16. d)–f): Electron diffraction patterns recorded on same Pb-doped samples.

structural modulation. Thirdly, it is possible to use the calculated $S_{2D}(k)$ to define a correlation length for the superlattice. More generally, the approach of calculating $S_{2D}(k)$ from real-space images enables the quantitative determination of local crystalline order and should thus be of great utility in materials science (for example, in comparing local microstructures and optimizing growth conditions).

4.4. Oxygen Doping: Probing Local Electronic Structure

It is widely recognized that oxygen doping plays a key role in determining the properties of oxide superconductors.[61, 62] The results from a number of studies have shown that variations in

oxygen concentration change the average carrier concentration and thereby the superconducting transition temperature. X-ray photoemission spectroscopy (PES) studies of BSCCO-2212 crystals doped at high oxygen pressure showed that the density of states near the Fermi level increases with increasing oxygen concentration.[80] To explain this increase in the density of states it has been suggested that oxygen doping transforms the BiO structural element into a metallic layer. The PES interpretation is complicated, however, by the fact that this technique probes several unit cells in depth. STM is uniquely suited to elucidating the origin of high-pressure doping, since it can probe directly the surface BiO layer's electronic states with little contribution form the underlying CuO_2 planes.

STM spectroscopy data obtained on as-grown and oxygen-annealed BSCCO crystals exhibit distinctly different $I-U$ behavior for the different oxygen treatments (Fig. 18),[81-83] attributable to distinctly different electronic structures near the

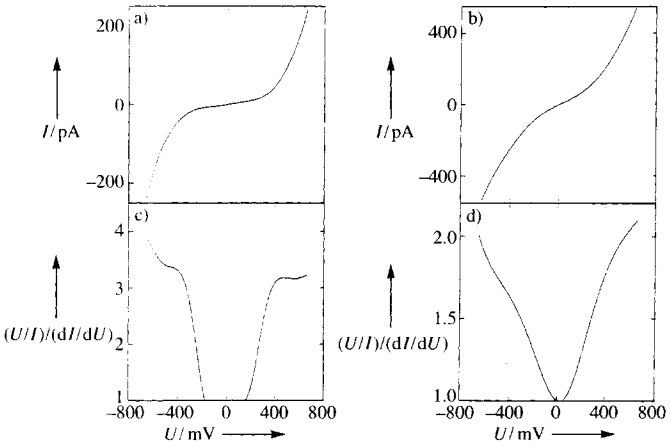

Fig. 18. Current versus voltage data (a, b) and normalized conductivity curves (c, d) obtained on as-grown (a, c) and oxygen-annealed (b, d) BSCCO-2212 single crystal samples.

Fermi level. The as-grown crystals exhibit a low current within ± 200 mV of E_f and relatively sharp increases in I beyond these points, while the oxygen-annealed samples show a smooth increase in I for all U. Indeed, the normalized conductivity $(U/I)\mathrm{d}I/\mathrm{d}U$ shows that there is a 330 mV gap in BiO layer density of states for the as-grown sample, but no obvious gap for the oxygen-annealed sample. The absence of a gap in the oxygen-annealed samples suggests that oxygen doping introduces impurity states into the gap or causes the BiO layer to become metallic.

STM imaging of the BiO layer atomic structure has provided additional information helping to resolve these two possibilities.[82] Atomic resolution images of the as-grown and oxygen-annealed samples exhibit the same surface atomic structure (Fig. 19). The lattices for the samples have periods of 3.8 ± 0.2 Å that corresponds to either the Bi–Bi or O–O distances. The observation of alternate lattice sites for a range of bias conditions indicates that the BiO layer is semiconducting in both as-grown and oxygen-annealed crystals. These structural results combined with the spectroscopic measurements thus suggest that the BiO layer's density of states increases with oxygen annealing, although this layer does not become metallic.

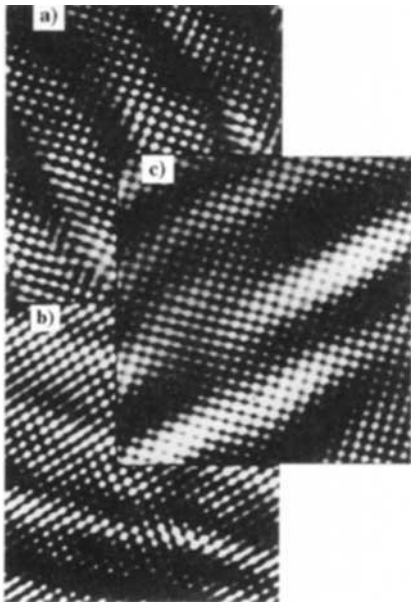

Fig. 19. STM images (10×10 nm^2) recorded on BSCCO crystals. Sample preparation: a) as-grown, b) annealed under 12 atm oxygen, and c) annealed under 150 atm oxygen.

4.5. The Superconducting Energy Gap

The spectroscopic capabilities of STM have also been exploited by many research groups to study the superconducting state of the high-T_c copper oxide materials.[84] The emphasis in this work has been to probe the superconducting energy gap (2Δ) and low-energy excitations in these materials, since this information is essential to understanding the mechanism of superconductivity. In the conventional Bardeen, Cooper, and Schrieffer (BCS) model of superconductivity, there is a complete gap in the density of electronic states as the temperature approaches 0, and the magnitude of 2Δ has the universal value of $3.53\,kT_c$.[85] For conventional superconductors these predictions have agreed well with measurements of the density of states by tunneling spectroscopy.[84, 86] In the case of the copper oxide materials, however, tunneling spectroscopy measurements have led to suggested values of 2Δ between 0 and $12\,kT_c$, although recent studies have converged towards an energy scale of $5-8\,kT_c$.[84, 87-90] It is likely that material inhomogeneity, such as oxygen nonstoichiometry, have been responsible for many of the apparently conflicting measurements of 2Δ by tunneling spectroscopy,[88-91] since the short coherence lengths of the copper oxide materials make these measurements especially susceptible to local variations in the superconducting properties. Indeed, spatially resolved spectroscopy measurements have shown clear evidence for variations in 2Δ associated with structural inhomogeneity.[88, 89]

To delineate the intrinsic versus extrinsic features of the superconducting energy gap in the high-T_c materials we have reported systematic measurements on carefully annealed BSCCO-2212 samples with T_c values ranging from 79 to 92 K. The STM spectroscopy measurements exhibited values of 2Δ that were uniform over the sample surfaces (Fig. 20). The $I-U$ curves recorded on crystals with T_c values of 79, 86, and 92 K all exhibit similar features including a relatively flat low-current

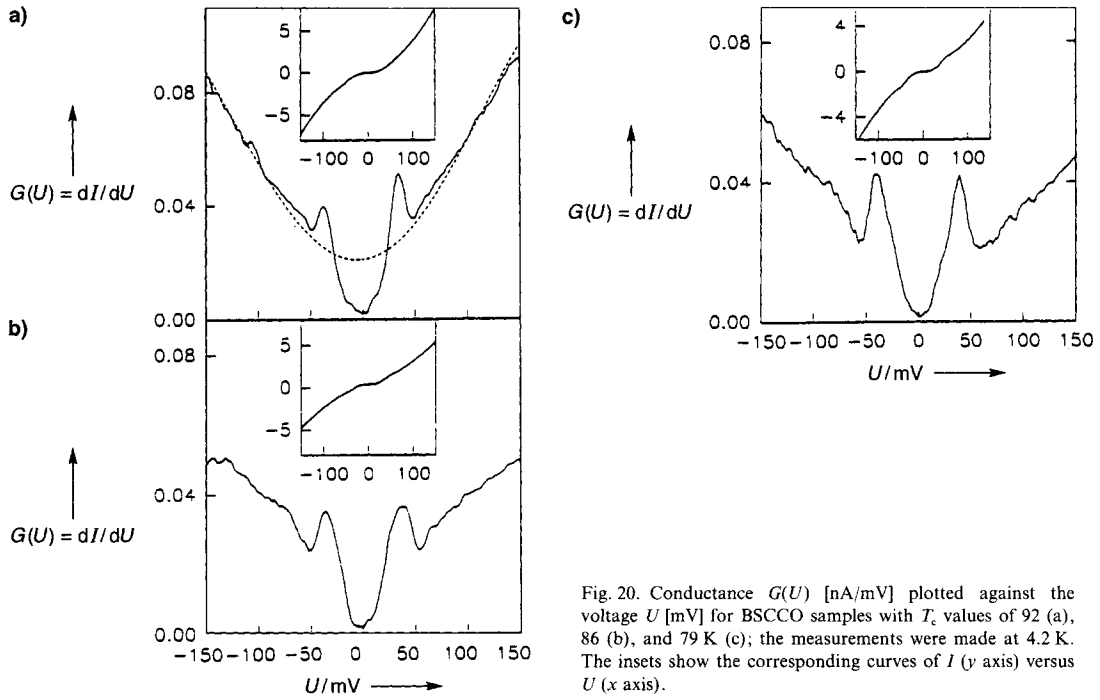

Fig. 20. Conductance $G(U)$ [nA/mV] plotted against the voltage U [mV] for BSCCO samples with T_c values of 92 (a), 86 (b), and 79 K (c); the measurements were made at 4.2 K. The insets show the corresponding curves of I (y axis) versus U (x axis).

region about $U = 0$ and pronounced conductance onsets at $\pm(20-25)$ mV. These features agree qualitatively with those expected for a superconducting gap. Clear insight into the electronic spectrum of the BSCCO samples in the superconducting state was obtained from the conductance $G(U)$, since it is proportional to the density of states N_S. The $G(U)$ vs. U curves obtained on the samples with T_c values varying from 79 to 92 K all showed similar features (Fig. 20). Reproducible features reported in these tunneling spectra include excitations within the gap region for $|U| > 0$ and well-defined conductance peaks. Significantly, the magnitudes of 2Δ determined from this data are similar, irrespective of the sample T_c.[90] These results demonstrate that 2Δ does not scale with T_c as found previously with conventional superconductors and thus have important implications regarding the mechanism of superconductivity.[90]

These data have also afforded the opportunity to examine in detail the quasi-particle excitations within the gap region (Fig. 21). Such an analysis is important, since it can provide insight into the symmetry of the energy gap function. Several models have been used to fit the tunneling spectroscopy data including the broadened BCS s-wave, the gapless, and the d-wave models. The broadened BCS function (g) does not provide

$$\frac{N_S}{N_N} = \mathrm{Re}\left\{\frac{\varepsilon}{\sqrt{\varepsilon^2 - \Delta^2}}\right\} \qquad (g)$$

($\varepsilon = eV - i\Gamma$, where V is the applied voltage and Γ a broadening parameter that reflects the finite lifetimes of quasi-particles)

a good fit of the experimental data, since it cannot simultaneously have sharp conductance peaks and excitations within the gap (Fig. 21 a). Hence, it is not expected to provide new insight into the physics of pairing. Alternatively, strong pair-breaking can lead to quasi-particle excitations within the gap. The long-dashed line in Figure 21 b was fit using a small amount of pair breaking ($\alpha = \Gamma/\Delta = 0.05$, where α is the pair-breaking parameter), while the short-dashed line corresponds to the behavior expected for a gapless superconductor ($\alpha = 1$). For s-wave symmetry pairing, previous theoretical studies have shown that as inelastic scattering is increased, the conductance peaks broaden and the observed gap ω_g gets smaller, but until the "gapless" regime is reached, no quasi-particle excitations should be observed within the gap.[92] In the context of s-wave pairing, this description is inconsistent with the observation of sharp conductance peaks.

The fact that $G(U)$ is strongly peaked around $\pm\Delta$ and decreases gradually to a minimum at $U = 0$ strongly suggests that there are nodes in the gap function. A function with d-wave symmetry (for example, $d_{x^2-y^2}$: $\Delta(k) \sim \cos k_x a - \cos k_y a$) is one that will have nodes and also has the symmetry that in several theoretical models is a prerequisite for pairing. Significantly, good agreement was obtained by fitting the energy-dependent density of states predicted for gap functions with d-wave symmetry to the tunneling spectroscopy data (Fig. 21 c, d).[90] The fit in Figure 21 c corresponds to the function of N_S/N_N expected for a pure d-wave symmetry gap, while that in Figure 21 d corresponds to the specific d-wave pairing model of

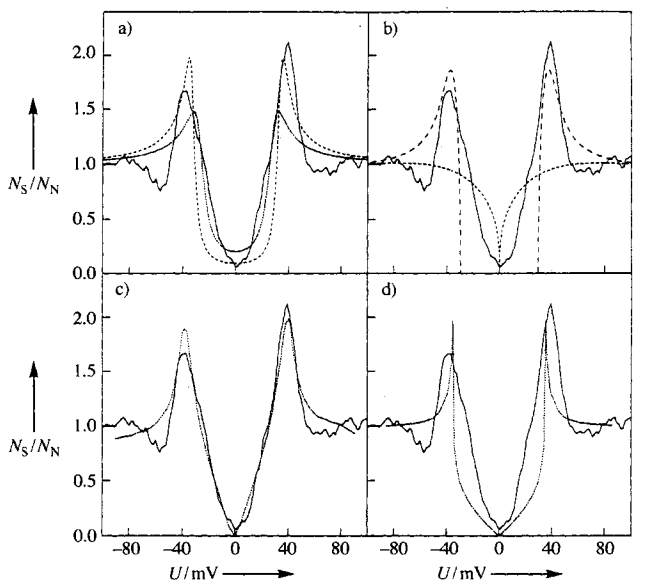

Fig. 21. Curve fitting to typical normalized conductance N_S/N_N versus voltage U data. In all cases the solid curve corresponds to the experimental data and the dashed lines to the fits. The fits were made with Equation (a), varying Δ and Γ in a) and α in b). The curve in c) represents a pure d-wave superconductors, and that in d) the d-wave model of Monthoux, Balatsky, and Pines.

Monthoux, Balatsky, and Pines.[93] Hence, the tunneling data strongly support the idea of an anisotropic gap function, but does not distinguish conclusively between d-wave and anisotropic s-wave models.

4.6. Magnetic Flux-Lines

When a type-II superconductor, such as a material of the copper oxide family, is placed in a sufficiently large field, magnetic flux penetrates through the sample in the form of quantized magnetic flux-lines called vortices.[95, 96] In the absence of crystal defects and pinning the vortices are expected to be arranged in a hexagonal lattice that minimizes the repulsive interaction between lines. This hexagonal structure was recorded beautifully in STM images of flux-line arrays in $NbSe_2$ (Fig. 22).[97] In contrast, when pinning is present, the flux-line lattice structure will change to maximize the pinning interaction, and defects are balanced against the elastic deformation energy expended to distort the lattice.[95, 96]

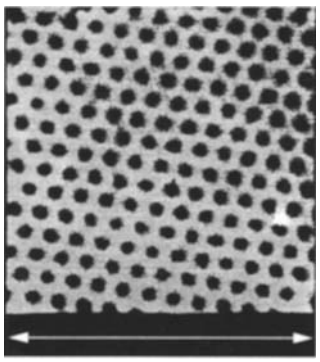

Fig. 22. STM image of the magnetic flux-line lattice in $NbSe_2$ at a field of 1 Tesla. The data were recorded at 1.8 K [97]. The arrow represents 6000 Å.

Surface and bulk defects can play an important role in pinning magnetic flux-lines in high-T_c materials.[95, 96, 98, 99] Because flux-line pinning determines to large extent the magnitude of J_c in superconductors (and therefore possible applications), an understanding of pinning is central to much work in the high-T_c field. Several techniques, including Bitter decoration and neutron diffraction, have been used to study the structure of flux-line lattices in the copper oxide materials.[95, 98] While both of these techniques have provided significant insight into the structure of flux-line lattices, they have not been able to provide direct information about the defects that pin the flux-lines. A new approach that we have developed combining conventional Bitter decoration and AFM has yielded significant insight into this critical area.[100] Bitter decoration is a well-established technique for highlighting reproducibly large numbers of flux-lines, and when combined with AFM, enables us to image the decorated flux-line positions and map out surface defects with a resolution of nanometers. Typical AFM images obtained on BSCCO single crystals that had been decorated in a magnetic field of 33 G are shown in Figure 23. Two distinct types of structures are seen in these images: the magnetic flux-line positions, which appear as small circular spots, and surface steps that appear as lines running through each image. Analysis of the surface topography demonstrates that these steps have heights of 30, 100, and 300 nm. Importantly, we have shown that the flux-line lattice structure can differ significantly depending on the surface step height.[100]

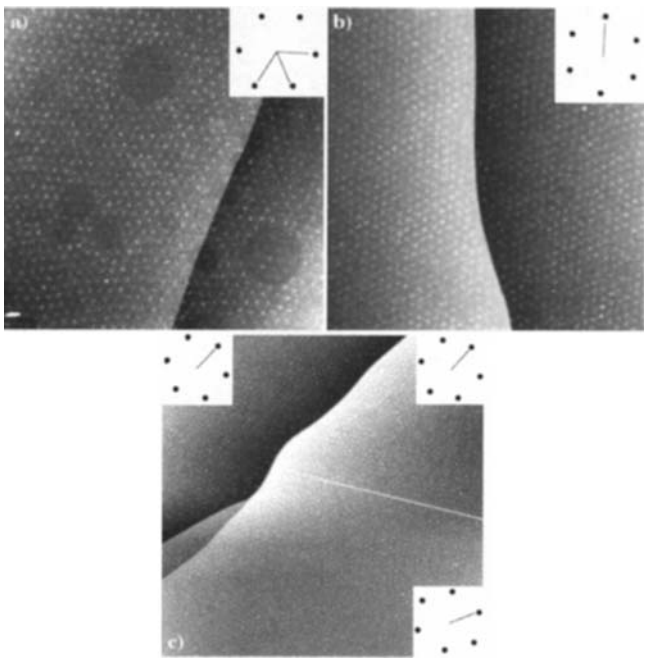

Fig. 23. AFM images recorded on a BSCCO crystal that was decorated at 4.2 K in a magnetic field of 33 Gauss. See text for further details.

The flux-line lattice orientation is seen most clearly in two-dimensional Fourier transform power spectra (2DFT) of selected regions of these images. The 2DFT, which are plotted as insets in each of the figures, each exhibit six diffraction spots characteristic of the hexagonal symmetry of the flux-line lattice and orientation defined by the reciprocal lattice vectors. In Figure 23a, the flux-line lattice orientation is independent of the surface step as is clearly evident when comparing the flux-line lattice reciprocal lattice vectors with the step direction. In Figure 23b, which contains a larger step, the 2DFT shows that a principle axis of the flux-line lattice is aligned preferentially along the straight section of the step. The overall orientation of the flux-line lattice is not perturbed, however, by the curvature in the step at the bottom of the image. The structure of the flux-line lattice in Figure 23c, which contains the largest step, is more complex and interesting. On the lower surface terrace in the upper left of the image, the 2DFT shows that the flux-line lattice orientation is pinned to the step direction. The flux-line lattice in the upper right portion of the image is also pinned in this same orientation. However, the 2DFT demonstrates that the flux-line lattice orientation in the lower part of the image is rotated relative to the upper part. This rotation follows the change in step direction that occurs at the bottom of the image. Significantly, the two distinct flux-line lattice orientations lead to the formation of a grain boundary in the lattice that is indicated by the white line running across the right side of this image. We have developed a model to understand the propagation of these grain boundaries through a sample by considering the pinning energy associated with the surface step and the energy required to elastically deform the flux-lattice.[98] Importantly, using the AFM data it has been possible to demonstrate that the grain boundaries propagate completely through the superconductor samples and thus influence significantly the bulk structure of the flux-line lattice.

5. Manipulation of Matter

5.1. New Nanomaterials Using SPMs

SPM techniques can, in addition to probing the microscopic properties of low-dimensional materials, be used to create new low-dimensional materials—nanostructures. SPM techniques are particularly powerful in nanoscale research, since they can be exploited for both the synthesis and the characterization of a material.[13, 14, 101-113] For example, STM has been used to assemble individual iron atoms into circular structures on a copper metal surface, and to show that the resulting structure exhibited properties of quantum confinement.[111]

The simplicity and flexibility of SPM techniques are a significant advantage for the synthesis and characterization of nanostructures. STM and AFM tips may be coated with thin films of almost any material thereby enabling researchers to control interactions and reactions at substrate surfaces.[114, 115] Experiments may also be carried out in vacuum or in ambient or fluid environments. Such flexibility is not possible in other top down lithography techniques.

5.2. General Approaches to Manipulation

SPM techniques have been used extensively to modify surfaces at the atomic to nanometer scale.[13, 14, 101-113] While modification of a surface in and of itself does not constitute the preparation of a nanostructure, an understanding of the processes involved in modification and manipulation are needed to prepare new structures rationally. Below we describe several processes that have been employed in STM and AFM studies.

Two general types of processes that have been used for STM-based manipulation involve the parallel or perpendicular motion of atoms and clusters (Fig. 24).[14a] In parallel processes, manipulated material is not removed from a surface but rather slid to a particular surface location. In perpendicular processes, however, the probe tip is used to pick up material from the surface and then redeposit it at another location. Parallel processes rely on either electric fields or chemical forces to slide atoms. An electric field emanating from a STM tip induces a dipole in adsorbates that attract them to the tip.[14a, 107] When this attraction is greater than the potential barrier associated with the dipole's moving across a surface, the adsorbate will move towards the tip. An advantage of this technique is that it enables both sample manipulation and the measurement of the dipole moment of an adsorbate. A second parallel process exploits short range attractive interactions between the probe tip and adsorbate to overcome the barrier to surface motion.

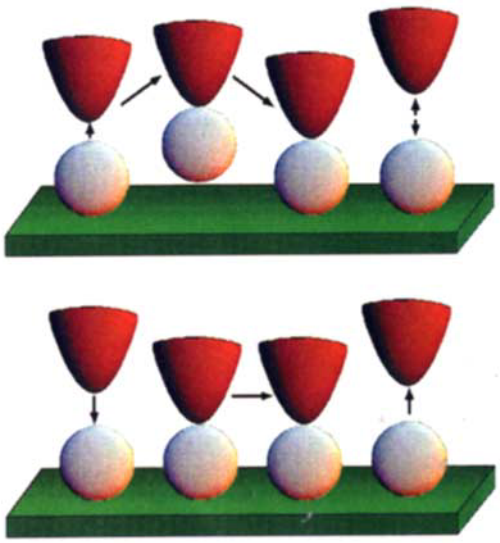

Fig. 24. Schematic diagram illustrating perpendicular (top) and parallel (bottom) manipulation processes.

The principal perpendicular processes are field evaporation and transfer-on-contact. The simpler of the two is transfer-on-contact whereby the tip is lowered onto an atom or cluster so that tip interacts strongly with the surface adsorbate.[14] As the tip is lifted from the surface, it carries the atom or cluster with it. At a desired location the tip is again lowered until the atom or cluster transfers back to the surface. The second type of perpendicular process involves field evaporation or chemically assisted field evaporation.[14, 106, 109] Field evaporation occurs when a large positive bias is applied to the sample (or tip) causing positive cluster ions to evaporate and ideally redeposit on the tip (or sample). An important example of this approach has been the selective removal and deposition small silicon clusters on the surface of crystalline silicon.[106]

AFM modification and manipulation processes are generally more direct than those for the STM. Manipulation based on force microscopy typically involves direct mechanical interactions between the probe tip and substrate. Force microscopy has been used to manipulate materials both by nanomachining[104, 110, 116] and sliding.[112, 113] In nanomachining, the AFM removes atoms from the surface through fatigue wear.[110, 117] For example, the pattern of letters "MoO_3" shown in Figure 25 was machined in a MoO_3 nanocrystal with an AFM probe tip.

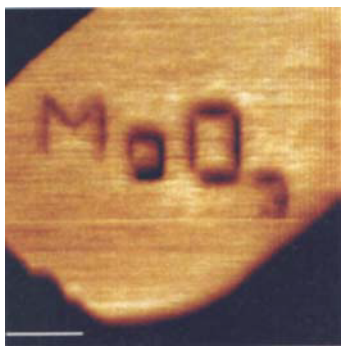

Fig. 25. AFM image engraved with "MoO_3". The pattern of letters was machined in a MoO_3 nanocrystal using the AFM probe tip.

The mechanics of the interaction between tip and sample that is relevant to nanomachining are illustrated in Figure 26. The tip elastically deforms due to the applied load, where the dashed line in the figure shows the shape of the nondeformed tip. A detailed view of the stresses felt by the sample are shown in the zoom of the tip–sample contact region (Fig. 26, right). The upper half of the zoom shows that the pressure distribution felt by the surface, while the lower half shows the stresses in the sample. The maximum stress occurs at a depth of $0.48/a$ below the surface, where a is proportional the radius of curvature of the tip. Under sufficient stress the sample will plastically deform, bonds will break, and material will be lost. All the material in the region may be removed by scanning the tip over it several times. Practical considerations limit the materials that may be machined in this way. The material should be softer than the tip and should not

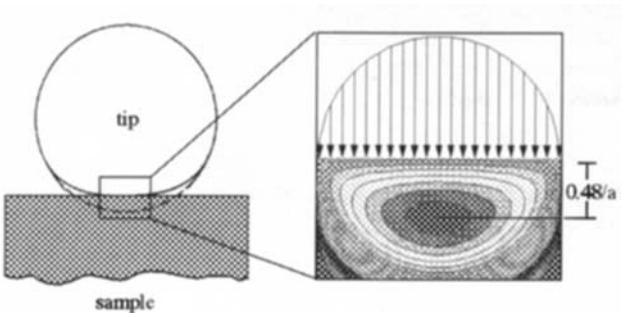

Fig. 26. Illustration of an AFM tip in contact with a surface. Left: The tip elastically deforms on the surface. Right: The arrows represent the pressure experienced by the surface and the gray hatched regions the stresses in the surface. See text for further details.

have of low friction coefficient. A soft material is needed, so that the tip may reproducibly modify the sample and not be modified itself, while a high friction coefficient ensures high interfacial shear and hence large transfer of energy.

The second means of AFM manipulation involves sliding small islands of material on a surface with the AFM's tip.[112, 113] A particularly interesting example of sliding is the phenomenon of lattice-directed sliding that we have recently discovered while manipulating nanocrystals of MoO_3 on MoS_2.[113] MoO_3 nanocrystals can be grown on the surface of MoS_2 by controlled thermal oxidation.[110] When these nanocrystals are pushed with an AFM tip, they move along only one of the lattice directions of the underlying MoS_2 substrate. The motion of two distinct MoO_3 nanocrystals are illustrated in the sequence of images shown in Figure 27a–c.[113] A composite view of these three images and the underlying MoS_2 atomic lattice (Fig. 27d) shows that these two nanocrystals move at a 60° angle with respect to each other and that this motion is along two distinct directions of the MoS_2 lattice. Under most conditions the MoO_3 nanocrystal will slide on this predetermined path indefinitely. The nanocrystals path can be changed, however, by applying a large torque using the tip. Hence, by combining lattice directed sliding with nanomachining it should be possible to construct complex multicomponent nanostructures.

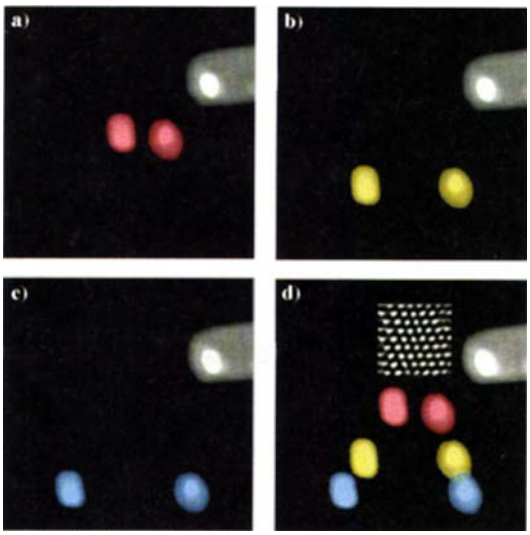

Fig. 27. AFM images showing the lattice-directed sliding of two MoO_3 nanocrystals on a MoS_2 surface. The red (a), white (b), and blue (c) colors correspond to the initial, intermediate, and final positions of the nanocrystals, respectively. d) Depicts a superposition of a), b), and c). The inset shows the atomic lattice of MoS_2.

5.3. Nanostructures

We now turn to two exciting examples of complex nanostructures that have been *synthesized* with the STM and AFM. One of the most elegant structures created with STM is the "quantum corral" built by Eigler and co-workers (Fig. 28).[111] Using a low-temperature (4 K) STM operating in ultrahigh vacuum, they slid 48 Fe atoms into a 14.3 nm ring on a Cu(111) surface. This ring of atoms acted as a hard wall, reflecting electrons trapped in a two-dimensional state at the surface of the copper substrate. The quantum-mechanical interference between these electrons created circular regions of high and low electron density (Fig. 28d).[111] Structures like the quantum corral, though currently limited to low temperature and high vacuum, are solid steps forward in quantum electronics research.

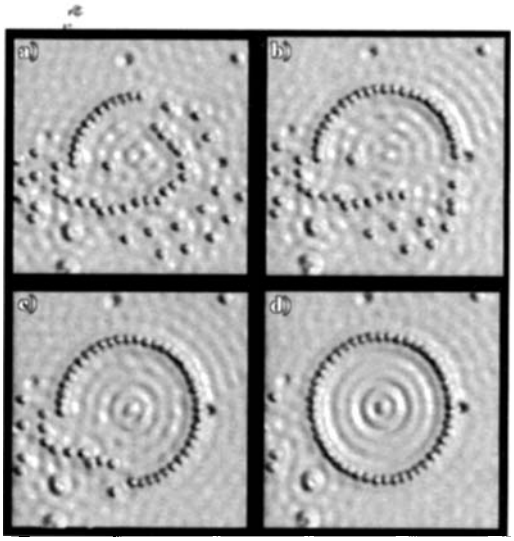

Fig. 28. Steps a) -d) in the formation of a quantum corral [111]. The corral has a radius of 14.3 nm and was created with parallel processes in STM manipulation. In d) the surface electron waves scatter from the Fe atoms leaving fringes.

We have used AFM to create an interlocking nanostructure that is stable at room temperature by combining nanomachining and lattice-directed sliding to manipulate MoO_3 nanocrystals on MoS_2 (Fig. 29).[113] Initially, nanomachining is used to define a notch in crystal 2 (Fig. 29b) and a rectangular latch in crystal 1 (Fig. 29c). Lattice-directed sliding is used to move crystal 2 to crystal 1 (Fig. 29c) and then move the latch into the notch of crystal 2 (Fig. 29d). The smaller crystallite is thereby locked into place by the latch. The preferred lattice-directed sliding directions of the small crystallite and the latch are different, which prevents the small crystallite from moving. The latch itself is prevented from rotating by the large crystallite. An interesting feature of this system is the reversibility of the connection. The smaller nanocrystal may be locked into place, unlocked, manipulated, and then relocked. This is exactly what has oc-

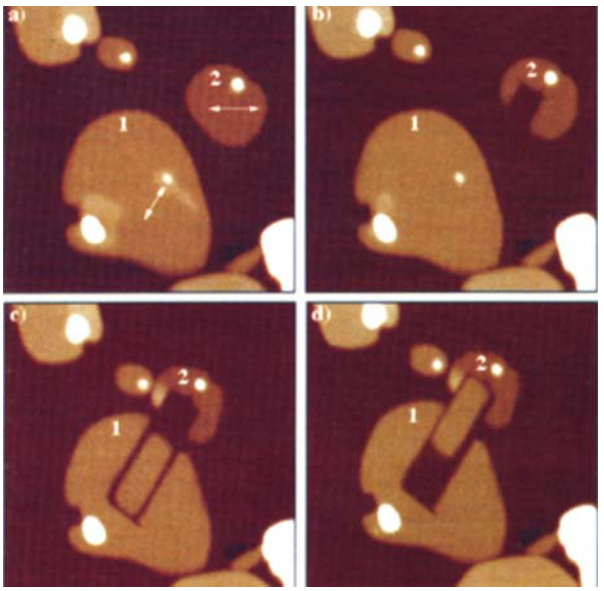

Fig. 29. AFM images illustrating the fabrication and final structure of three interlocking MoO_3 nanocrystals. See text for further details.

curred in Figures 29 c and d. This locking mechanism can, however, readily resist motion, relative to the larger crystal, of the small nanocrystal along its preferred sliding direction. Hence, the lock can be used as a structure to facilitate the fabrication of larger, more complicated systems that include, for example, electronically distinct oxide pieces. In addition, such a mechanical latch corresponds to the basic components needed to construct a nano logic gate.

6. Summary and Outlook

The combination of scanning probe microscopies and chemical synthesis has significantly advanced the understanding of charge density waves, high-temperature superconductivity, and nanofabrication in low-dimensional materials. This new approach to studying materials has directly elucidated the structure of complex charge density wave phases and how metal dopants interact with charge density waves in two-dimensional metal dichalcogenide solids. The real-space picture of atomic and charge density wave lattices provided by STM transforms the diffuse structural view based on diffraction into one that has demonstrated clearly the theoretical concept of weak pinning and has led to discovery of new phases not yet understood theoretically. The coupling of STM with synthesis has also illuminated complex structural disorder in two distinct classes of copper oxide superconductors, thus providing an understanding of observed variations in the bulk transition temperature and critical current density. The methods developed to quantify structural disorder in these studies—termed local crystallography—provide an approach for preparing pure and doped crystals that are homogeneous on a nanometer scale and should be of general utility in the future. Application of this approach to the superconducting state has elucidated details of the electronic excitations important in defining the mechanism of superconductivity and also the structure of magnetic flux-line arrays that are crucial to most technological applications. Such studies are, however, still in their infancy and will require additional work to broaden their impact. Lastly, the combination of scanning probe microscopy measurement and manipulation with chemical synthesis has provided a novel route to the fabrication of nanostructures (which represent the ultimate dimensional reduction in materials). Selective synthesis yields nanocrystals that have, through fundamental studies of friction and wear, been selectively modified and manipulated using force microscopy into interlocking, multicomponent structures. By using this strategy it should be possible to extend nanostructure complexity, and importantly, to readily investigate the physical properties of any new structure created with the probe microscope. More generally, the studies outlined in this review provide a clear pathway to unify work on bulk low-dimensional materials and nanostructures and our understanding of these solids, and in so doing they promise to expand our knowledge and our ability to conceive of new materials for the future.

Received: August 18, 1995 [A 132 IE]
German version: *Angew. Chem.* **1996**, *108*, 748–768

[1] G. Binnig, H. Rohrer, C. Gerber, E. Weibel, *Phys. Rev. Lett.* **1982**, *49*, 57–60.
[2] Introductions: a) *Scanning Tunneling Microscopy* (Eds.: J. A. Stroscio, W. J. Kaiser), Academic Press, New York, **1993**; b) *Scanning Tunneling Microscopy I* (Eds.: H.-J. Guntherodt, R. Wiesendanger), Springer, New York, **1992**; c) *Scanning Tunneling Microscopy II* (Eds.: R. Wiesendanger, H.-J. Guntherodt), Springer, New York, **1992**; d) *Scanning Tunneling Microscopy III* (Eds.: R. Wiesendanger, H.-J. Guntherodt), Springer, New York, **1993**; e) C. J. Chen, *Introduction to Scanning Tunneling Microscopy*, Oxford University Press, New York, **1993**.
[3] G. Binnig, H. Rohrer, *Sci. Am.* **1985**, *256*, 50–56; C. F. Quate, *Phys. Today* **1986**, *39*, 26–33; G. Binnig, H. Rohrer, *Angew. Chem.* **1987**, *99*, 622–631; *Angew. Chem. Int. Ed. Engl.* **1987**, *26*, 606–614; P. K. Hansma, J. Tersoff, *J. Appl. Phys.* **1987**, *61*, R1–R23; Y. Kuk, P. J. Silverman, *Rev. Sci. Instrum.* **1989**, *60*, 165–180; J. E. Griffith, G. P. Kochanski, *Annu. Rev. Mater. Sci.* **1990**, *20*, 219–244; Ph. Avouris, *J. Phys. Chem.* **1990**, *94*, 2246–2256.
[4] J. Frommer, *Angew. Chem.* **1992**, *104*, 1325–1357; *Angew. Chem. Int. Ed. Engl.* **1992**, *31*, 1298–1328.
[5] P. K. Hansma, V. B. Elings, O. Marti, C. E. Bracker, *Science* **1988**, *242*, 209–242.
[6] S. N. Magonov, M.-H. Whangbo, *Adv. Mater.* **1994**, *6*, 355–371.
[7] C. M. Lieber, *Chem. Eng. News* **1994**, *72*, 28–41; X. L. Wu, C. M. Lieber, *Prog. Inorg. Chem.* **1991**, *39*, 431–510; C. M. Lieber, X. L. Wu, *Acc. Chem. Res.* **1991**, *24*, 170–177.
[8] H. Dai, C. M. Lieber, *Annu. Rev. Phys. Chem.* **1993**, *44*, 237–263.
[9] J. A. Golovchenko, *Science* **1986**, *232*, 48–53; R. M. Tromp, R. J. Hamers, J. E. Demuth, *Science* **1986**, *234*, 304–309.
[10] G. Binnig, C. F. Quate, C. Gerber, *Phys. Rev. Lett.* **1986**, *56*, 930–933.
[11] D. Sarid, *Scanning Force Microscopy*, Oxford University Press, New York, **1994**.
[12] B. Drake, C. B. Prater, A. L. Weisenhorn, S. A. C. Gould, T. R. Albrecht, C. F. Quate, D. S. Cannell, H. G. Hansma, P. K. Hansma, *Science* **1989**, *243*, 1586–1589; D. Ruger, P. Hansma, *Phys. Today* **1990**, *October*, 23–30; S. M. Hues, R. J. Colton, E. Meyer, H.-J. Guntherodt, *MRS Bull.* **1993**, *18*, 41–49; C. F. Quate, *Surf. Sci.* **1994**, *299/300*, 980–995.
[13] *Technology of Proximal Probe Lithography* (Eds.: C. R. K. Marrian), SPIE Optical Engineering Press, Bellingham, WA, **1993**; *Atomic and Nanometer-Scale Modification of Materials: Fundamentals and Applications* (Ed.: Ph. Avouris), Kluwer, Boston, **1993**.
[14] a) J. A. Stroscio, D. M. Eigler, *Science* **1991**, *254*, 1319–1326; Ph. Avouris, *Acc. Chem. Res.* **1994**, *27*, 159–165; b) Ph. Avouris, *ibid.* **1995**, *28*, 95–102.
[15] J. C. Patrin, J. H. Weaver, *Phys. Rev. B* **1993**, *48*, 17913–17921; D. Rioux, R. J. Pechman, M. Chander, J. H. Weaver, *ibid.* **1994**, *50*, 4430–4438.
[16] K. Koguchi, T. Matsumoto, T. Kawai, *Science* **1995**, *267*, 71–73.
[17] M. Kanai, T. Kanai, K. Motui, X. D. Wang, T. Hashizume, T. Sakurai, *Surf. Sci.* **1995**, *329*, L619–623; X. D. Wang, T. Hashizume, T. Sakurai, *Mod. Phys. Lett. B* **1994**, *8*, 1597–1626.
[18] J. Tersoff, D. R. Hamann, *Phys. Rev. Lett.* **1983**, *50*, 1998–2001; J. Tersoff, D. R. Hamann, *Phys. Rev. B* **1985**, *31*, 805–813; J. Tersorff, N. D. Lang in Ref. [2a], 1–29.
[19] J. Bardeen, *Phys. Rev. Lett.* **1961**, *6*, 57–59.
[20] J. Tersoff, *Phys. Rev. B* **1990**, *41*, 1235–1238.

[21] J. Tersoff, *Phys. Rev. B* **1989**, *40*, 11990–11993.
[22] N. D. Lang, *Phys. Rev. Lett.* **1986**, *56*, 1164–1167; H. J. Unger, *Comput. Mater. Sci.* **1994**, *2*, 357–365.
[23] R. M. Feenstra, J. A. Stroscio, A. P. Fein, *Surf. Sci.* **1987**, *181*, 295–306.
[24] E. Meyer, H. Heinzelmann in Ref. [2c], 99–149.
[25] E. C. Teague, G. E. Scire, S. M. Baker, S. W. Jensen, *Wear* **1982**, *83*, 1.
[26] J. A. Wilson, A. D. Yoffe, *Adv. Phys.* **1969**, *18*, 193–335; R. M. A. Lieth, J. C. J. M. Terhell in *Preparation and Crystal Growth of Materials with Layered Structures* (Ed.: R. M. A. Lieth), D. Reidel Publishing Co., Dordrecht, **1977**, p. 141.
[27] J. A. Wilson, F. J. DiSalvo, S. Mahajan, *Adv. Phys.* **1975**, *24*, 117–201.
[28] F. J. DiSalvo in *Electron-Phonon Interactions and Phase Transitions* (Ed.: T. Riste), New York, **1977**.
[29] R. L. Withers, J. A. Wilson, *J. Phys. C: Solid State Phys.* **1986**, *19*, 4809–4845.
[30] K. Nakanishi, H. Takatera, Y. Yamada, H. Shiba, *J. Phys. Soc. Jpn.* **1977**, *43*, 1509–1517; K. Nakanishi, H. Shiba, *ibid.* **1977**, *43*, 1839–1847.
[31] C. B. Scruby, P. M. Williams, G. S. Parry, *Philos. Mag.* **1975**, *31*, 255–275; G. Brusdeylins, C. Heimlich, J. P. Toennies, *Surf. Sci.* **1989**, *211/212*, 98–105.
[32] R. V. Coleman, B. Drake, P. K. Hansma, G. Slough, *Phys. Rev. Lett.* **1985**, *55*, 394–397.
[33] R. V. Coleman, B. Giambattista, P. K. Hansma, A. Johnson, W. W. McNairy, C. G. Slough, *Adv. Phys.* **1988**, *37*, 559–644.
[34] Xian Liang Wu and Charles M. Lieber, *Science* **1989**, *243*, 1703–1705.
[35] Xian Liang Wu and Charles M. Lieber, *Phys. Rev. Lett.* **1990**, *64*, 1150–1153.
[36] R. E. Thomson, U. Walter, E. Ganz, J. Clarke, A. Zettl, *Phys. Rev. B* **1988**, *38*, 10734–10743.
[37] B. Giambattista, C. G. Slough, W. W. McNairy, R. V. Coleman, *Phys. Rev. B* **1990**, *41*, 10082–10103; C. G. Slough, W. W. McNairy, R. V. Coleman, J. Garnaes, C. B. Prater, P. K. Hansma, *ibid.* **1990**, *42*, 9255–9258.
[38] B. Burk, R. E. Thomson, A. Zettl, J. Clarke, *Phys. Rev. Lett.* **1991**, *66*, 3040–3043.
[39] G. Grunner, *Rev. Mod. Phys.* **1988**, *60*, 1129–1181; G. Grunner, A. Zettl, *Phys. Rep.* **1985**, *119*, 117–232.
[40] F. J. DiSalvo, J. A. Wilson, B. G. Bagley, J. V. Waszczak, *Phys. Rev. B* **1975**, *12*, 2220–2235.
[41] H. Fukuyama, P. A. Lee, *Phys. Rev. B* **1978**, *17*, 535–548.
[42] P. A. Lee, T. M. Rice, *Phys. Rev. B* **1979**, *19*, 3970–3980.
[43] S. N. Coppersmith, *Phys. Rev. Lett.* **1990**, *65*, 1044–1047.
[44] J. R. Tucker, *Phys. Rev. B* **1989**, *40*, 5447–5459.
[45] J. Bardeen, *Phys. Rev. Lett.* **1990**, *64*, 2297–2299.
[46] E. Sweetland, C.-Y. Tsai, B. A. Wintner, J. D. Brocker, R. E. Thorne, *Phys. Rev. Lett.* **1990**, *65*, 3165–3168.
[47] J. R. Tucker, *Phys. Rev. Lett.* **1990**, *65*, 270–273.
[48] J. C. Gill, *Phys. Rev. Lett.* **1990**, *65*, 271–272.
[49] R. E. Thorne, J. McCarten, *Phys. Rev. Lett.* **1990**, *65*, 273.
[50] X. L. Wu, P. Zou, C. M. Lieber, *Phys. Rev. Lett.* **1988**, *61*, 2604–2607.
[51] H. Chen, X. L. Wu, C. M. Lieber, *J. Am. Chem. Soc.* **1990**, *112*, 3326–3332.
[52] X. L. Wu, C. M. Lieber, *J. Am. Chem. Soc.* **1989**, *111*, 2731–2733.
[53] H. Dai, H. Chen, C. M. Lieber, *Phys. Rev. Lett.* **1991**, *66*, 3183–3186.
[54] X. L. Wu, C. M. Lieber, *Phys. Rev. B* **1990**, *41*, 1239–1242.
[55] H. Dai, C. M. Lieber, *Phys. Rev. Lett.* **1992**, *69*, 1576–1579.
[56] X. Wu, P. Zhou, C. M. Lieber, *Nature* **1988**, *335*, 55–57.
[57] H. Dai, C. M. Lieber, *J. Phys. Chem.* **1993**, *97*, 2362–2367.
[58] F. R. N. Nabarro, *Theory of Dislocations*, Dover, New York, **1967**.
[59] D. R. Nelson, M. Rubinstein, F. Spaepen, *Philos. Mag. A* **1982**, *46*, 105–126.
[60] B. I. Halperin, D. R. Nelson, *Phys. Rev. Lett.* **1978**, *41*, 121–124; D. R. Nelson, B. I. Halperin, *Phys. Rev. B* **1979**, *19*, 2457–2484.
[61] B. Raveau, C. Michel, M. Hervieu, D. Groult, *Crystal Chemistry of High-Tc Superconducting Copper Oxides*, Springer, Berlin, **1991**; *Chemistry of Superconductor Materials* (Ed.: T. A. Vanderah), Noyes Publications, Park Ridge, New Jersey, **1991**.
[62] A. W. Sleight, *Science* **1988**, *242*, 1519–1527; I. K. Schuller, J. D. Jorgensen, *Mater. Res. Soc. Bull.* **1989**, *14*, 27–30.
[63] C. N. R. Rao, B. Raveau, *Acc. Chem. Res.* **1989**, *22*, 106–113; B. Raveau, C. Michel, *Annu. Rev. Mater. Sci.* **1989**, *19*, 319–339; H. Müller-Buschbaum, *Angew. Chem.* **1989**, *101*, 1503–1524; *Angew. Chem. Int. Ed. Engl.* **1989**, *28*, 1472–1493; R. J. Cava, *Science* **1990**, *247*, 656–662.
[64] Y. Gao, P. Lee, P. Coppens, M. A. Subramanian, A. W. Sleight, *Science* **1988**, *241*, 954–956; C. Patterson, P. D. Hatton, R. J. Nelmes, X. Chu, Y. F. Yan, Z. X. Zhao, *Supercond. Sci. Technol.* **1990**, *3*, 297–301.
[65] P. Lee, Y. Gao, H. S. Sheu, V. Petricek, R. Restori, P. Coppens, A. Darovskikh, J. C. Phillips, A. W. Sleight, M. A. Subramanian, *Science* **1989**, *244*, 62–63.
[66] M. D. Kirk, J. Nogami, A. A. Baski, D. B. Mitzi, A. Kapitulnik, T. H. Geballe, C. F. Quate, *Science* **1988**, *242*, 1673–1675.
[67] X. L. Wu, Z. Zhang, Y. L. Wang, C. M. Lieber, *Science* **1990**, *248*, 1211–1214.
[68] C. K. Shih, R. M. Feenstra, G. V. Chandrashekhar, *Phys. Rev. B* **1991**, *43*, 7913–7922; A. Chang, Y. M. Ivanchenko, Z. Y. Rong, E. L. Wolf, *Surf. Sci.* **1992**, *274*, L504–L508; K. Ikeda, K. Takamuku, K. Yamaguchi, R. Itti, N. Koshizuka, *J. Mater. Res.* **1992**, *7*, 1060–1062.
[69] Y. Yamamoto, M. Onoda, E. Takayama-Muromachi, F. Izumi, *Phys. Rev. B* **1990**, *42*, 4228–4239; V. Petricek, Y. Gao, P. Lee, P. Coppens, *ibid.* **1990**, *42*, 387–392.
[70] H. W. Zandbergen, W. A. Groen, F. C. Mijlhoff, G. van Tendeloo, S. Amelinckx, *Physica C* **1988**, *156*, 325–354; H. W. Zandbergen, W. T. Fu, G. van Tendeloo, S. Amelinckx, *J. Cryst. Growth* **1989**, *96*, 716–725; O. Eibl, *Physica C* **1991**, *175*, 419–434.
[71] X.-L. Wu, C. M. Lieber, D. S. Ginley, R. J. Baughman, *Appl. Phys. Lett.* **1989**, *55*, 2129–2131; Z. Zhang, C. M. Lieber, D. S. Ginley, R. J. Baughman, B. Morosin, *J. Vac. Sci. Technol. B* **1991** *9*, 1009–1012.
[72] Z. Zhang, C.-C. Chen, C. M. Lieber, B. Morosin, D. S. Ginley, E. L. Venturini, *Phys. Rev. B* **1992**, *45*, 987–992.
[73] D. E. Cox, C. C. Torardi, M. A. Subramanian, J. Gopalakrishnan, A. W. Sleight, *Phys. Rev. B* **1988**, *38*, 6624–6630; C. C. Torardi, M. A. Subramanian, J. C. Calabrese, J. Gopalakrishnan, K. J. Morrissey, T. R. Askew, R. B. Flippen, U. Chowdhry, A. W. Sleight, *Science* **1988**, *240*, 631–634.
[74] D. S. Ginley, B. Morosin, R. J. Baughman, E. L. Venturini, J. E. Schirber, J. F. Kwak, *J. Crystal Growth* **1988**, *91*, 456–462; B. Morosin, R. J. Baughman, D. S. Ginley, J. E. Schirber, E. L. Venturini, *Physica C* **1990**, *161*, 115–124; B. Morosin, D. S. Ginley, E. L. Venturini, R. J. Baughman, C. P. Tigges, *ibid.* **1991**, *172*, 413–422.
[75] Z. Zhang, Y. L. Wang, X. L. Wu, J.-L. Huang, C. M. Lieber, *Phys. Rev. B* **1990**, *42*, 1082–1085.
[76] J. Liu, C. M. Lieber, *Inorg. Chim. Acta*, in press.
[77] C. H. Chen, D. J. Werder, G. P. Espinosa, A. S. Cooper, *Phys. Rev. B* **1989**, *39*, 4686–4689; J. Schneck, L. Pierre, J. C. Toledano, C. Daguet, *ibid.* **1989**, *39*, 9624–9627.
[78] Y. L. Wang, X. L. Wu, C.-C. Chen, C. M. Lieber, *Proc. Natl. Acad. Sci.* **1990**, *87*, 7058–7061.
[79] C. C. Torardi, E. M. McCarron, P. L. Gai, J. B. Parise, J. Ghoroghchian, D. B. Kang, M.-H. Whangbo, J. C. Barry, *Physica C* **1991**, *176*, 347–356; K. Yanagisawa, Y. Matsui, K. Shoda, E. Takayama-Muromachi, S. Horiuchi, *ibid.* **1992**, *196*, 34–42.
[80] B. O. Wells, Z.-X. Shen, D. S. Dessau, W. E. Spicer, C. G. Olson, D. B. Mitzi, A. Kapitulnik, R. S. List, A. Arko, *Phys. Rev. Lett.* **1990**, *65*, 3056–3059; b) Z.-X. Shen, D. S. Dessau, B. O. Well, C. G. Olson, D. B. Mitzi, L. Lombado, R. S. List, A. J. Arko, *Phys. Rev. B* **1991**, *44*, 12098–12101.
[81] X. L. Wu, Y. L. Wang, Z. Zhang, C. M. Lieber, *Phys. Rev. B* **1991**, *43*, 8729–8732.
[82] Z. Zhang, C. M. Lieber, *Phys. Rev. B* **1992**, *46*, 5845–5848.
[83] Z. Zhang, C. M. Lieber, *J. Phys. Chem.* **1992**, *96*, 2030–2038.
[84] J. R. Kirtley, *Int. J. Mod. Phys. B* **1990**, *4*, 201–237; T. Haegawa, H. Ikuta, K. Kitazawa in *Physical Properties of High Temperature Superconductors III* (Ed.: D. M. Ginsberg), World Scientific Publishing, River Edge, NJ, **1992**, p. 525.
[85] J. Bardeen, L. N. Cooper, J. R. Schrieffer, *Phys. Rev.* **1957**, *108*, 1175–1204.
[86] I. Giaever, K. Megerle, *Phys. Rev.* **1961**, *122*, 1101–1111.
[87] Z. Zhang, C. M. Lieber, *Phys. Rev. B* **1993**, *47*, 3423–3426; Y. Li, J. Liu, C. M. Lieber, *Phys. Rev. Lett.* **1993**, *70*, 3494–3497.
[88] E. L. Wolf, A. Chang, Z. Y. Rong, Y. M. Ivanchenko, F. Lu, *J. Supercond.* **1994**, *7*, 355–360.
[89] C. Renner, O. Fischer, *Phys. Rev. B* **1995**, *51*, 9208–9218.
[90] J. Liu, Y. Li, C. M. Lieber, *Phys. Rev. B* **1994**, *49*, 6234–6238.
[91] J.-X. Liu, J.-C. Wan, A. M. Goldman, Y. C. Chang, P. Z. Jiang, *Phys. Rev. Lett.* **1991**, *67*, 2195–2198; H. J. Tao, A. Chang, F. Lu, E. L. Wolf, *Phys. Rev. B* **1992**, *45*, 10622–10632.
[92] K. Maki in *Superconductivity* (Ed.: R. D. Parks), Dekker, New York, **1969**, p. 1035.
[93] P. Monthoux, A. V. Balatsky, D. Pines, *Phys. Rev. Lett.* **1991**, *67*, 3448–3451; P. Monthoux, A. V. Balatsky, D. Pines, *Phys. Rev. B* **1992**, *46*, 14803–14817.
[94] C. Jiang, J. P. Carbotte, R. C. Dynes, *Phys. Rev. B* **1993**, *47*, 5325–5331.
[95] D. J. Bishop, P. L. Gammel, D. A. Huse, C. A. Murray, *Science* **1992**, *255*, 165–172; D. A. Huse, M. P. A. Fisher, D. S. Fisher, *Nature* **1992**, *358*, 553–559.
[96] R. P. Huebener, *Magnetic Flux Structures in Superconductors*, Springer, New York, **1979**.
[97] H. F. Hess, R. B. Robinson, R. C. Dynes, J. M. Valles, J. V. Waszczak, *Phys. Rev. Lett.* **1989**, *62*, 214–216; H. F. Hess, C. A. Murray, J. V. Waszczak, *Phys. Rev. B* **1994**, *50*, 16528–16540.
[98] H. Dai, J. Liu, C. M. Lieber, *Phys. Rev. Lett.* **1994**, *72*, 748–751.
[99] H. Dai, S. Yoon, J. Liu, R. C. Budhani, C. M. Lieber, *Science* **1994**, *265*, 1552–1556; S. Behler, P. Jess, A. Baratoff, H. J. Guntherodt, *Physica C* **1994**, *235–240*, 2703–2704.
[100] S. Yoon, H. Dai, J. Liu, C. M. Lieber, *Science* **1994**, *265*, 215–218.
[101] F. Grey, *Adv. Mater.* **1993**, *5*, 704–710.
[102] P. Bedrossian, D. M. Chen, K. Mortensen, J. A. Golovchenko, *Nature* **1989**, *342*, 258–260.
[103] Y. Utsugi, *Nature* **1990**, *347*, 747–749; H. J. Mamin, D. Rugar, *Appl. Phys. Lett.* **1992**, *61*, 1003–1005; A. Sato, Y. Tsukamoto, *Nature* **1993**, *363*, 431–432.

[104] E. Garfunkel, G. Rudd, D. Novak, S. Wang, G. Ebert, M. Greenblatt, T. Gustafsson, S. H. Garofalini, *Science* **1989**, *246*, 99–100; S. Miyake, *Appl. Phys. Lett.* **1994**, *65*, 980–982.
[105] D. M. Eigler, E. K. Schweizer, *Nature* **1990**, *344*, 524–526; D. M. Eigler, P. S. Weiss, E. K. Schweizer, N. D. Lang, *Phys. Rev. Lett.* **1991**, *66*, 1189–1192.
[106] I.-W. Lyo, Ph. Avouris, *Science* **1991**, *253*, 173–176; C. T. Salling, M. G. Lagally, *ibid.* **1994**, *265*, 502–506; A. Kobayashi, F. Grey, R. S. Williams, M. Aono, *ibid.* **1993**, *259*, 1724–1726.
[107] L. J. Whitman, J. A. Stroscio, R. A. Dragoset, R. J. Celotta, *ibid.* **1991**, *251*, 1206–1210.
[108] C. M. Lieber, Y. Kim, *Thin Solid Films* **1991**, *206*, 355–359; Y. Kim, J.-L. Huang, C. M. Lieber, *Appl. Phys. Lett.* **1991**, *59*, 3404–3406; E. Delawski, B. A. Parkinson, *J. Am. Chem. Soc.* **1992**, *114*, 1661–1667.
[109] J.-L. Huang, Y.-E. Sung, C. M. Lieber, *Appl. Phys. Lett.* **1992**, *61*, 1528–1530; S. Akari, R. Moller, K. Dransfeld, *ibid.* **1991**, *59*, 243–245.
[110] Y. Kim, C. M. Lieber, *Science* **1992**, *257*, 375–377; C. M. Lieber, Y. Kim, *Adv. Mater.* **1993**, *5*, 392–394.
[111] M. F. Crommie, C. P. Lutz, D. M. Eigler, *Science* **1993**, *262*, 218–220.
[112] R. Lüthi, E. Meyer, H. Haefke, L. Howald, W. Gutmannsbauer, H.-J. Güntherodt, *Science* **1994**, *266*, 1979–1982.
[113] P. E. Sheehan, C. M. Lieber, *Science*, submitted.
[114] C. D. Frisbie, L. F. Rozsnyai, A. Noy, M. S. Wrighton, C. M. Lieber, *Science* **1994**, *265*, 2071–2073; A. Noy, C. D. Frisbie, L. F. Rozsnyai, M. S. Wrighton, C. M. Lieber, *J. Am. Chem. Soc.* **1995**, *117*, 7943–7951.
[115] W. T. Muller, D. L. Klein, T. Lee, J. Clarke, P. L. McEuen, P. G. Schultz, *Science* **1995**, *268*, 272–273; S. J. O'Shea, R. M. Atta, M. E. Welland, *Rev. Sci. Instrum.* **1995**, *66*, 2508–2512.
[116] J. Hu, X.-D. Xiao, D. F. Ogletree, M. Salmeron, *Surf. Sci.* **1995**, *327*, 358–370.
[117] U. Landman, W. D. Luedtke, N. Burnham, R. J. Colton, *Science* **1990**, *248*, 454–461.

EVENTS

IRaP 96

2nd International Symposium on Ionizing Radiation and Polymers

Nov. 3-8, 1996, Saint-François, Guadeloupe, FWI

IRaP96 is the second symposium of an international series devoted to ionizing radiation effects in polymers. IRaP conferences bring together scientists from research, universities and industries involved in radiation polymer science. Their aim is to facilitate the exchange of knowledge and information in this cross-disciplinary field and to promote innovative industrial applications. The topics will cover fundamental process, surface and bulk modifications, advanced materials and technological applications. Furthermore, IRaP96 will highlight the influence of ionizing radiation on the modification of chemical and physical properties (e.g. electrical, mechanical, optical, tribological, diffusion...). In addition to electron, photon and ion beam effects, studies with lasers and cluster beams in polymers will be included.

The program consists of keynote lectures, invited and contributed talks, and posters.

A particular attention is given to new materials which can find applications in medecine, biology, biotechnology, defense, environmental protection, and energy saving.

For more information and registration (before September the 15th), please contact:

Dr. Natacha BETZ
Chairwoman of IRaP 96 organizing committee
DRECAM/SRSIM/LPI
CEA/Saclay
F - 91191 Gif sur Yvette Cedex
tel.: (33) 1 69 08 48 34 ; fax : (33) 1 69 08 96 00
e-mail : betz@drecam.cea.fr.; irap@drecam.cea.fr